ACCEPTED MANUSCRIPT

This is the author's peer reviewed, accepted manuscript. However, the online version of record will be different from this version once it has been copyedited and typeset.
PLEASE CITE THIS ARTICLE AS DOI: 10.1063/5.0336473

Journal of Applied Physics

AIP Publishing

# Absolute Doubly Differential Angular Sputtering Yields for 20 keV $Kr^+$ Impacting a Loose Cu Powder

Caixia Bu[1]*, Sebastien Verkercke[2,3]*, Deborah Berhanu[4], Benjamin C. Bostick[5], Steven N. Chillrud[5], Benjamin A. Clouter-Gergen[6], Denton S. Ebel[5,7], Isabel Hahn[8], George E. Harlow[7], Pierre-Michel Hillenbrand[9], Dmitry A. Ivanov[1], Jesse R. Lewis[6], Liam S. Morrissey[6,7]*, James M. Ross[5], Xavier Urbain[10] and Daniel W. Savin[1]*

[1] Columbia Astrophysics Laboratory, Columbia University, New York, NY 10027, USA.
[2] Laboratoire de Physique des Plasmas/CNRS, École polytechnique, Palaiseau, France.
[3] Centre National d'Études Spatiales, Paris, France
[4] Department of Science and Mathematics, Fashion Institute of Technology, New York, NY 10001, USA.
[5] Lamont-Doherty Earth Observatory, Columbia University, Palisades, NY 10964, USA.
[6] Memorial University of Newfoundland, St. John's NLA1C 5S7, Canada.
[7] American Museum of Natural History, New York, NY 10024, USA.
[8] Pomona College, Claremont, CA 91711, USA.
[9] GSI Helmholtzzentrum für Schwerionenforschung, 64291, Darmstadt, Germany
[10] Université catholique de Louvain, B-1348 Louvain-la-Neuve, Belgium

*Corresponding Authors: caixiabu@gmail.com; sebastien.verkercke@latmos.ipsl.fr; lsm088@mun.ca; dws26@columbia.edu.

## Abstract

We have measured the absolute doubly differential angular sputtering yield for 20 keV $Kr^+$ impacting a loose Cu powder at an incidence angle of $\theta_i = 45°$. We find that ion sputtering from a loose Cu powder differs dramatically from a flat Cu slab under the same irradiation conditions, being most pronounced for the angular distribution. The ejecta lobe for the powder is directed primarily backwards, relative to the ion velocity vector. This contrasts with the slab, where the lobe is peaked nearly normal to the surface. We attribute the backward directed ejecta lobe to two effects. First, ions can penetrate through the interconnected voids of the powder and cause sputtering from underlying grains. Atoms sputtered from these underlying grains are most likely to escape the powder if they are ejected roughly toward the origin of the incident ions, while ejecta in other directions are more likely to be shadowed by neighboring grains. Second, for $\theta_i = 45°$, the grain surfaces exposed to the ions are primarily oriented in the backward direction, leading to shadowing of forward directed ejecta. We find qualitatively good agreement between our experimental measurements and the results of our multiscale Monte Carlo simulation of sputtering from granular targets. We attribute the remaining discrepancies to ion-induced surface modifications not included in the simulations. Our findings indicate that ion sputtering from loose powders is distinctly different from that of flat surfaces, rough surfaces, and pressed powders due to the lack of interconnected voids in these latter three targets.

ACCEPTED MANUSCRIPT
Journal of Applied Physics
AIP Publishing
This is the author's peer reviewed, accepted manuscript. However, the online version of record will be different from this version once it has been copyedited and typeset.
PLEASE CITE THIS ARTICLE AS DOI: 10.1063/5.0336473

## 1 Introduction

Ion sputtering of loose powders is important in disparate fields such as thin film deposition and planetary science. In thin film deposition, the use of powder targets, as opposed to slab targets, offers significant advancements in semiconductor manufacturing through reduced costs, flexible combination of compositions, and improved film uniformity and quality [1 – 3]. In planetary science, solar wind ions and cosmic rays irradiate the regolith surfaces of airless planetary bodies, such as the Moon, Mercury, and asteroids [4 – 7]. Ion sputtering of the regolith plays a significant role in the surface alteration and exosphere formation of these bodies [8 – 13].

Advances in these fields required knowing the total sputtering yield, which is defined as the number of sputtered atoms per incident ion, as well as the doubly differential angular sputtering yield, which is the number of sputtered atoms per incident ion per steradian. When considering powder targets, it is also important to take into account the granular nature of the bulk sample, the porosity (defined as the ratio of void volume to the total volume, noting that the void volume includes both the space between the grains and any space that may exist inside the grains), and the surface roughness of the individual grains. The granular nature results in a porous bulk surface topography with a peak-to-valley height on the order of the grain size diameters. We defined this as "granular roughness" to distinguish it from the surface roughness of an individual grain or of a non-porous solid. In addition, the interconnected voids of the granular structure enables ions to penetrate below the surface layer and produce sputtering from underlying layers. These properties can potentially increase the redeposition rate of the sputtered atoms sputtered from a loose powder as compared to a non-porous rough surface. Hence, the behavior of ion sputtering from powders can differ significantly from sputtering of slabs, the latter of which have been extensively studied experimentally and theoretically [14 – 16]. The same cannot be said for ion sputtering from loose powders.

Experimentally, powder studies in the 1960s and 1970s focused not on sputtering yields but on the optical properties of the irradiated material, finding that loosely packed powders darkened, but that pressed pellets (formed from loose powders) and flat slabs remained light in color [4]. These results suggest that sputtering studies using pellets and slabs are not accurate analogs for sputtering from powders. Furthermore, these early studies attributed the darkening, in part, to the ejecta being redeposited onto the loose powder, but they did not attempt to quantify sputtering yields or the percentage of ejecta retained by the powder. This subject was revisited by two later experimental studies that provided rough estimates for the percentage of the ejecta retained but still did not provide sputtering yields. Hapke and Cassidy [17] irradiated a loosely-packed and lightly-sintered basaltic glass powder with ions and estimated that over 90% of the ejecta was redeposited (i.e. retained) within the powder. Loeffler et al. [18] irradiated a compressed powder pellet of olivine with ions and estimated that ~ 67% of the ejecta was redeposited into the pellet. The reasons for the difference are unclear. It might be due to the reference used. Hapke and Cassidy [17] referenced their powder results, with a grain size distribution finer than 37 μm, to results using a bead of 7 mm in diameter. Loeffler et al. [18] referenced their pressed pellet results to a flat slab. Other potential sources of difference include the different porosity of the loosely-packed versus compressed powder, the different sample compositions, the different sticking coefficients for the ejecta onto the powder, the formation of ion-induced surface roughness, or some other combination of unknowns.

ACCEPTED MANUSCRIPT
Journal of Applied Physics
AIP Publishing
This is the author's peer reviewed, accepted manuscript. However, the online version of record will be different from this version once it has been copyedited and typeset.
PLEASE CITE THIS ARTICLE AS DOI: 10.1063/5.0336473

Since that time, we are unaware of any additional experimental results on loose powders. However, there has been work recently on ion sputtering from pellets. The absolute mass sputtering yields have been reported for Mercury mineral analogs [19] and for a lunar soil [20]. The results were reported only for sputtering in the incidence plane, which is defined by the velocity vector of the impacting ions and the bulk normal to the surface. The pellets used were formed from grains with size diameters on the order of ~ 100 μm; but the pressing to form pellets is likely to have removed much of the granular roughness, as well as much of the porosity. As a result, those works primarily explore the effects of surface roughness on the ~ 1 μm scale, as can be seen from their measured surface topographies. Interestingly, though, the results do indicate that as surface roughness increases, so does the retention of the ejecta. This is suggestive that granularity and porosity might also increase the retention (i.e., decrease the sputtering yield).

Theoretically, until recently, the only detailed simulation for ion sputtering of powders has been that of Cassidy and Johnson [21]. That work predicted an ejecta escape rate of ~ 10 – 30%, for a sticking coefficient $S$ = 1. The lower end of the range corresponds to a forward-directed distribution of the ejecta (forward relative to the incident ion velocity vector) and the upper end to cosine-law dependence for the ejecta distribution. The escape rate increases as $S$ decreases. That work, though, made a number of simplifying theoretical approximations to make the calculations readily tractable, thereby limiting the ability to quantitatively apply those findings to laboratory measurements or other real world situations. It is only very recently that theoretical models have been developed that combine physically realistic state-of-the-art ion sputtering calculations with granular models that incorporate porosity [20, 22]. However, until our work reported here, no experimental data have been available to benchmark these new theoretical models.

Here, we have measured the absolute doubly differential angular sputtering yield from a loose Cu powder irradiated by 20 keV $Kr^+$ impacting at an incidence angle of $\theta_i = 45°$ relative to the bulk surface normal. Our study builds upon our earlier measurements using a Cu slab target [23]. Comparing the two sets of results enable us to investigate the effect of a porous powder structure on the sputtering process and to provide benchmarks for models simulating ion sputtering from loose powders.

The rest of this paper is organized as follows: Section 2 describes the experimental details. Section 3 briefly reviews the simulation model we have developed to investigate ion sputtering from loose powders. Section 4 presents and discusses the results. Finally, Section 5 summarizes our findings and their implications.

## 2 Experimental Methodology

### 2.1 Ion Irradiation

We irradiated a loose powder target with ions and collected the sputtered atoms using the experimental apparatus that we have recently developed [23, 24]. The apparatus is located at Columbia University Nevis Laboratories in Irvington, NY. One novel aspect of this apparatus is that the sample stage holding the target is mounted horizontally inside the target chamber. This orientation was specifically selected so as to enable sputtering studies of loose powders.

ACCEPTED MANUSCRIPT
Journal of Applied Physics
AIP Publishing
This is the author's peer reviewed, accepted manuscript. However, the online version of record will be different from this version once it has been copyedited and typeset.
PLEASE CITE THIS ARTICLE AS DOI: 10.1063/5.0336473

The irradiating $Kr^+$ was produced in a duoplasmatron [25], extracted at an energy of 20 keV to form a beam, and mass-to-charge selected using a Wien filter, in order to purify the beam by removing other ions produced in the source. Between the ion source and the target chamber, the beam was directed and shaped with multiple electrostatic lens, deflectors, and apertures. The extracted $Kr^+$ beam initially travelled horizontally ~ 2.5 m above the floor. It was then electrostatically deflected downward at an angle of 45° toward the target chamber. After this deflection, and before entering the target chamber, the ion beam was collimated by two 5-mm apertures placed ~ 1.2 meter apart. This enabled the day-to-day reproducibility of the beam shape on the irradiated sample. After entering the target chamber, the incident ions impacted the sample with a polar angle of $\theta_i = 45°$ with respect to the bulk surface normal. The target chamber base pressure was ~ $1 \times 10^{-8}$ Torr. During ion irradiation this increased to ~ $2 \times 10^{-8}$ Torr.

The ion beam shape, position, and current during irradiation were monitored by a single-wire beam profile monitor (BPM) [26], which was installed between the second aperture and the gate valve to the target chamber. The BPM readings were recorded every second. We calibrated the BPM current reading to the ion current measured by a Faraday cup positioned behind the sample stage location. This calibration enabled us to use the BPM signal to monitor the ion current in real time. The BPM current was calibrated before and after the ion-irradiation campaign, and the average of the calibration factors was used to calculate the total ion dose. The corresponding systematic uncertainty in the BPM calibration factor was 10%, which we attribute to changes in the surface properties of the BPM wire due to ion irradiation over the course of the measurement campaign. Here and throughout, all uncertainties are quoted at an estimated one-sigma confidence level.

The position of the ion beam on the sample stage was determined using an alumina scintillator before the irradiation campaign. We calibrated the BPM measurement of the beam position with the ion beam position on the scintillator, enabling us to use the BPM measurements to position the ion beam on the sample. Throughout the campaign, the center of the ion beam was within 0.3 mm of the center of the sample stage. Projecting the BPM measurements of the beam shape onto the sample stage, and accounting for $\theta_i$, the ion beam full width at half maximum (FWHM) on the target was ~ 5.4 mm in the incidence plane and ~ 4.0 mm in the perpendicular plane that passed through the sample center.

Before each day's irradiation, and with the gate valve closed to the target chamber, we used the BPM measurements to verify that the ion beam was properly positioned. The ion beam was then admitted into the target chamber. Typical irradiation currents were ~ 0.37 – 0.47 μA. Moderate retuning of the beam was sometimes required over the course of a day to compensate for a slow shift of the beam position with time, as is typical for beams produced in a duoplasmatron source. The sample was irradiated for a total of $6.51 \times 10^5$ s, over a period of 27 non-consecutive days, resulting in a total delivered dose of $(1.61 \pm 0.16) \times 10^{18}$ ions. This is about twice the dose that was used in [23]. The overall fluence was ~ $2.8 \times 10^{18}$ ions $cm^{-2}$, estimated using a beam area of ~ 0.57 $cm^2$ derived from the ion beam FWHM at the sample position. The systematic uncertainty of ~ 10% in the dose was due entirely to the BPM calibration. During ion irradiation, low energy electrons (< 5 eV) produced by a flood gun (Princeton Scientific FS40-PS) were used to prevent surface charging. This was necessary because the Cu powder behaves as an insulator due to the

ACCEPTED MANUSCRIPT
Journal of Applied Physics
AIP Publishing
This is the author's peer reviewed, accepted manuscript. However, the online version of record will be different from this version once it has been copyedited and typeset.
PLEASE CITE THIS ARTICLE AS DOI: 10.1063/5.0336473

high resistivity of the point contacts between the grains. The flood gun was turned on before ions were admitted into the target chamber. The electron current was ~ 8 μA and the electron beam size was ~ 2 times larger than the ion beam size, to cover completely the irradiated area.

## 2.2 Ejecta Collection

Sputtered atoms were accumulated using collectors distributed across a hemispherical dome above the sample. The collectors used to capture the sputtered atoms were circular, gold-coated quartz crystals with a diameter of 14 mm and were purchased from INFICON Inc. (model: 008-010-G10). These collectors were mounted on the openings of the dome, as shown in Fig. 1. Compared to the dome used in our previous study [23], the new dome was extended to span more than three-quarters of the solid angle above the sample, enabling us to investigate the symmetry of the sputtering yield with respect to the incidence plane. We also enlarged each opening from a diameter of 10 to 13 mm. Thus, each collector spanned a solid angle of $2.71 \times 10^{-2}$ sr. In addition, four witness collectors were mounted in the target chamber with no direct line of sight to the target. These were used to monitor for any potential mass gain resulting from the handling and atmospheric exposure of the collectors at various stages of the project.

A major uncertainty faced while planning the ion sputtering measurements from a loose powder was the predicted reduction in the sputtering yield. Based on the unbenchmarked theoretical work of [21], we expected sputtering yields ~ 10 – 30% of those in our previous slab results [23]. Collecting mass gains comparable to our previous work would have required as much as a factor of ten increase in campaign time, turning the previous 10 non-consecutive days of ion irradiation of [23] into an unrealistic 100 non-consecutive days. We compensated for this by reducing the desired mass gain to half and increasing the collector area by a factor of $(13/10)^2$. Together, these increased the predicted required total ion dose to twice that of our previous study, reducing the predicted campaign time to a more feasible ~ 30 non-consecutive days.

ACCEPTED MANUSCRIPT
Journal of Applied Physics
AIP Publishing
This is the author's peer reviewed, accepted manuscript. However, the online version of record will be different from this version once it has been copyedited and typeset.
PLEASE CITE THIS ARTICLE AS DOI: 10.1063/5.0336473

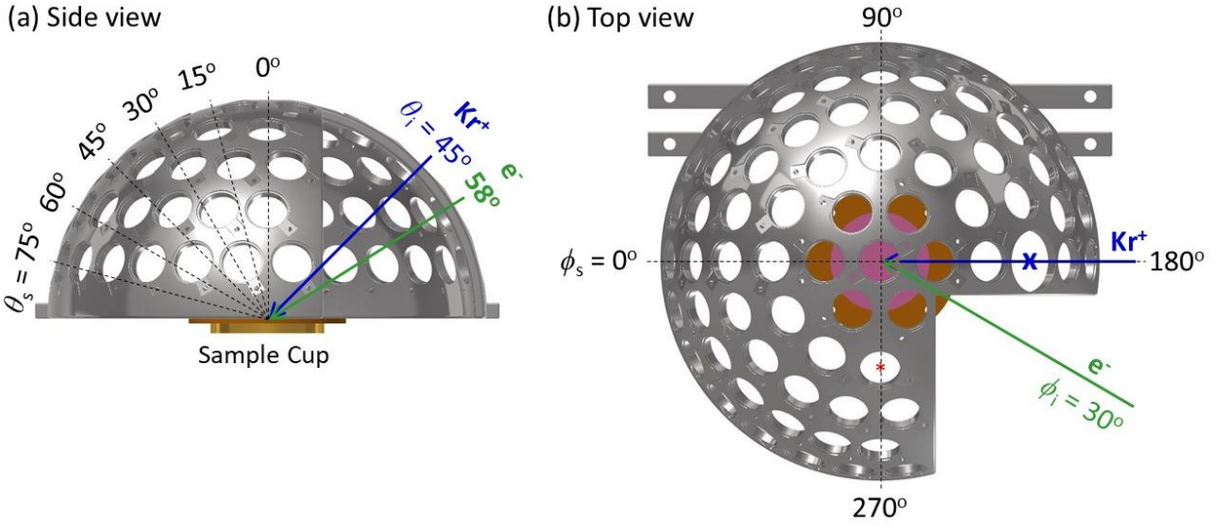



**Fig. 1.** Schematic of the dome used to hold the collectors. The collectors were mounted on the 13 mm diameter openings in the dome. The radial distance from the sample center to the center of each collector was 70 mm. (**a**) Side view showing the polar angles $\theta_i$ of the incident $Kr^+$ beam (blue arrow) and the flood gun electrons ($e^-$; green arrow), the polar angles $\theta_s$ of the collectors, and the sample cup. The polar angles are measured with respect to the bulk sample normal. One collector was situated at $\theta_s = 0°$. This was surrounded by rings of collectors at $\theta_s = 15°$, 30°, 45°, 60°, and 75°. Not all collector openings are visible in the figure. The collector locations are specified in detail in Section 4. (**b**) Top view showing the azimuthal angles of the $Kr^+$ and $e^-$ beams velocity vectors (blue and green arrows, respectively), the azimuthal angles $\phi_s$ for the collectors, and the Cu grains (magenta area). Here, $\phi_s = 0°$ is the direction of the ion beam velocity projected onto the bulk sample plane. The ions entered the dome through the opening marked with blue "×". The collectors in each $\theta_s$ ring spanned azimuthal sputtering angles $\phi_s$ from 0° to 360°, except for the opening for the $Kr^+$ beam at $(\theta_s, \phi_s) = (45°,180°)$, the wedge-shaped cut for the $e^-$ beam, and the opening at $(\theta_s, \phi_s) = (30°,270°)$ for visual inspection of the sample (this opening is marked with the red "∗").

ACCEPTED MANUSCRIPT
Journal of Applied Physics
AIP Publishing
This is the author's peer reviewed, accepted manuscript. However, the online version of record will be different from this version once it has been copyedited and typeset.
PLEASE CITE THIS ARTICLE AS DOI: 10.1063/5.0336473

### 2.3 Sample Preparation

For the sample to be studied, we used spherical, polycrystalline Cu grains of 99.9% purity (metals basis), from Thermo Fisher Scientific (Catalog number: 045544.22). The grains were sieved through electroformed stainless steel dry sieves (from Precision Eforming), and grains were selected with diameters of 53 – 90 μm (270 and 170 mesh, respectively). The grains as purchased, however, had been exposed to ambient atmosphere, and the formation of an oxidized surface layer was expected, consisting predominantly of cupric oxide (CuO) and/or cuprous oxide ($Cu_2O$) [27]. To purify this layer, we performed a chemical reduction of the sample using hydrogen ($H_2$) gas, a standard undergraduate chemistry laboratory exercise [28]. Briefly, the sieved grains were inserted into a glass tube. While $H_2$ flowed through the tube, the grains were heated for 10 minutes then cooled for 8 minutes. The heating activated reactions of both CuO and $Cu_2O$ with the $H_2$, forming $H_2O$ and removing the O from the sample. The heating and cooling process was repeated three times. The reduction was carried out in a laboratory at Columbia University's Lamont-Doherty Earth Observatory in Palisades, NY.

We then determined the porosity of the reduced Cu grains in the sample cup, which had a diameter of 32 mm and depth of 2 mm. We first weighed the sample cup. Afterwards, the Cu grains were poured into the sample cup and leveled using a stainless-steel spatula. Finally, we weighed the sample cup with the Cu grains. Combining the mass change and the volume of the sample cup, we derived the density of the Cu sample. The reduced-grain measurements were performed in a dry nitrogen ($N_2$) gas environment, in order to minimize the re-oxidization of the grains. The process was repeated three times; the average density of the Cu sample was $\rho_{powder} = 4.78 \pm 0.24$ g cm$^{-3}$. Using $\rho_{slab} = 8.9334 \pm 0.0002$ g cm$^{-3}$ as the density of the Cu slab [29], the porosity of the Cu powder sample is found to be $p = (\rho_{slab} - \rho_{powder}) / \rho_{slab} = 0.46 \pm 0.03$.

In a separate reduction campaign, we prepared reduced Cu grains for irradiation and characterization, following the same process as described above. Under a dry $N_2$ environment, the reduced grains were removed from the glass tube and poured into four separate glass vials, which were then sealed in individual bags inflated with dry $N_2$. After this, the samples were transported to the ion-irradiation laboratory.

In the ion-irradiation laboratory, one vial of the reduced grains was poured into the same sample cup and leveled using a stainless-steel spatula. The preparation of the sample for irradiation was identical to the density measurement above, and we assume that the sample has the same density and porosity. The sample cup was then mounted horizontally onto the sample stage inside the target chamber, and the target chamber evacuated. The time that the sample was exposed to air during this entire process was estimated to be less than 10 minutes. During this time, we exposed the other vials of reduced grains to the ambient laboratory environment, so that they would be representative of the sample to be irradiated. We dub these grains as the reference grains. Once the sample was mounted and the chamber evacuated, these reference vials were re-sealed in dry $N_2$ bags again for < 12 hours.

### 2.4 Sample Characterization

ACCEPTED MANUSCRIPT
Journal of Applied Physics
AIP Publishing
This is the author's peer reviewed, accepted manuscript. However, the online version of record will be different from this version once it has been copyedited and typeset.
PLEASE CITE THIS ARTICLE AS DOI: 10.1063/5.0336473

The sample references were transferred to various laboratories for characterization. The shape and bulk composition were determine using a scanning electron microscopy (SEM) integrated with energy dispersive spectroscopy (EDS). This system is located at the Fashion Institute of Technology, part of the State University of New York in Manhattan. Additional compositional information was measured using X-ray photoelectron spectroscopy (XPS) and X-ray diffraction (XRD). The XPS is based at the Advanced Science Research Center, located on the City College of New York campus in Manhattan. The XRD is located at the Columbia University Nano-Initiative Laboratory in Manhattan. The references experienced < 5 minutes of additional exposure to atmosphere while transferring from the glass vial into the SEM/EDS or XPS chambers. The XRD was done in ambient air; the characterization took ~ 10 minutes.

### 2.4.1 SEM measurements

The samples were imaged using the SEM. As expected, the majority of the grains were found to have a spherical shape, with diameters of 53 – 90 μm. This can be seen in Fig. 2(a) showing the low magnification SEM image of the reduced grains. Figure 2(b) is the high magnification SEM image for a representative grain, which shows the grain surface is relatively smooth, with some micrometer-scale blobs and patches on the surface. Within the SEM resolution, we did not detect changes in the grain shape or surface morphology between the as-received and reduced grains.

ACCEPTED MANUSCRIPT
Journal of Applied Physics
AIP Publishing
This is the author's peer reviewed, accepted manuscript. However, the online version of record will be different from this version once it has been copyedited and typeset.
PLEASE CITE THIS ARTICLE AS DOI: 10.1063/5.0336473

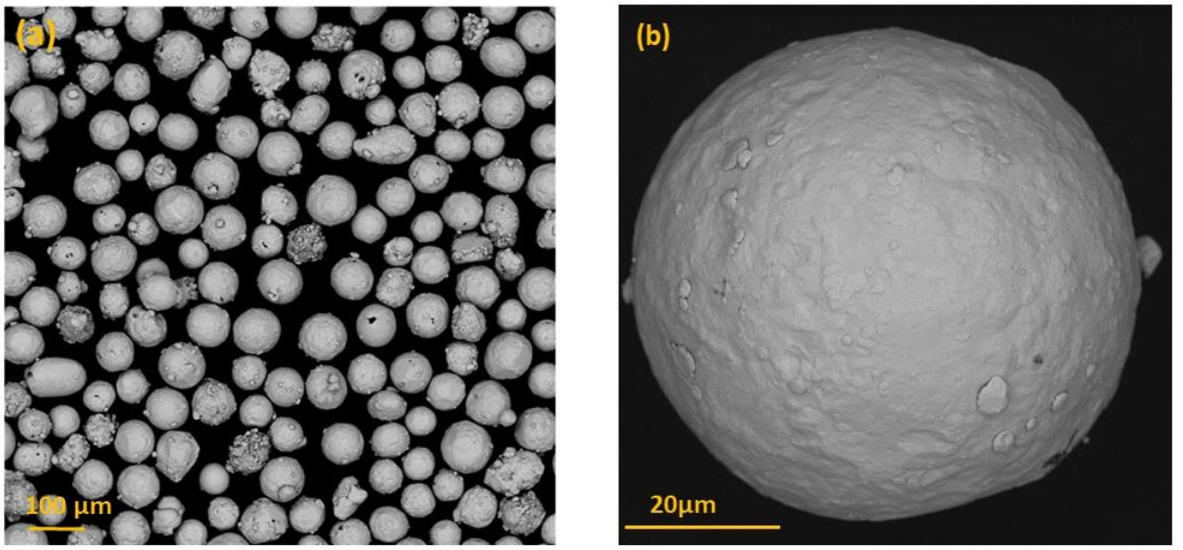



**Fig. 2.** (a) SEM image of Cu grains after reduction showing that the majority of the grains have a spherical shape, within the expected diameter range of 53 – 90 µm. (b) High magnification SEM image for a representative grain. The SEM images were collected on a Phenom XL using 5 keV primary electrons at a magnification of ×280 for (a) and ×2950 for (b).

ACCEPTED MANUSCRIPT
Journal of Applied Physics
AIP Publishing
This is the author's peer reviewed, accepted manuscript. However, the online version of record will be different from this version once it has been copyedited and typeset.
PLEASE CITE THIS ARTICLE AS DOI: 10.1063/5.0336473

### 2.4.2 XPS measurements

The surface composition of the reduced Cu grains was characterized with XPS, using a Physical Electronics Versaprobe II system equipped with a monochromated Al *K*α X-ray source and dual beam charge neutralization. XPS works by irradiating a sample with monochromatic X-rays and analyzing the kinetic energy of the ejected electrons. Direct ionization of a core electron produces photoelectrons with a kinetic energy given by $E_k = E_{X\text{-}ray} - E_B - \phi_w$. Here, $E_{X\text{-}ray} = 1486.6$ eV, $E_B$ is the binding energy of the core electron with respect to the Fermi level, and $\phi_w$ is the work function of the spectrometer. The X-rays can also produce Auger electrons through a process where first a core hole is created by excitation or ionization. The hole is then filled by an electron from a higher orbital and the energy released by this decay goes into ionizing another bound electron. Any remaining energy goes into kinetic energy of this Auger electron. Here, we observed the formation of Cu *L*-shell holes that were filled by an *M*-shell electron leading to the Auger emission of another *M*-shell electron, i.e., *LMM* Auger electrons.

Each element has unique binding energies for its core electrons. These energies are sensitive to the chemical environment of the atom [30]. Thus, the precise kinetic energy of the photoelectrons gives the information on the chemical state of the element, while the relative area of the photoelectron peaks, together with the instrumental sensitivity factors, is used to obtain elemental abundance [30]. The penetration depth of the photons into the solid is on the order of micrometers, with ionization occurring along the entire penetration length. However, only those electrons that originate from within a few nanometers below the surface produce analytically useful peaks in the kinetic energy spectrum, as these electrons leave the surface with minimal energy loss. Those electrons that originate from deeper below the surface undergo inelastic loss processes before emerging contribute to the energy spectrum background. Hence, XPS primarily probes surface properties. For the Cu grains used in our study here, the estimated inelastic mean free path is ~ 1 nm for the Cu-2*p* photoelectrons, ~ 2.5 nm for O-1*s*, and ~ 3 nm for the C-1*s* [31].

In our study, survey spectra were collected at a pass energy of 117.4 eV, providing an energy resolution of ~ 4 eV. Each survey spectrum took ~ 8 minutes, and provided a broad overview of the elements present in the top ~ 3 nm of our sample. In order to determine the chemical states of the Cu atoms, we also took high-energy-resolution (HR) spectra at the energies of the Cu-2*p*, O-1*s*, and C-1*s* photoelectrons, as well as of the Cu-*LMM* Auger electrons. The HR spectra were taken at a pass energy of 23.5 eV, providing an energy resolution of ~ 0.5 eV. Each HR spectra took ~ 30 minutes. Spectral analysis was performed using Multipak (Version 9.6.0). For all the spectra, we first calibrated the energy scale by setting the C-1*s* peak (adventitious carbon resulting from the brief exposure to ambient atmosphere during sample transferring) to a kinetic energy of 1201.8 eV (corresponding to a binding energy $E_B$ of 284.8 eV). For the quantitative analysis, we used the HR spectra after the subtraction of a Shirley background [32,33].

Figure 3 shows a representative XPS survey for the reduced Cu grains. Six Cu core-level peaks are readily identifiable in the spectrum: the Cu-2*p* doublet spanning a kinetic energy of ~ 535 – 555 eV (corresponding to $E_B \approx 932 - 952$ eV), Cu-3*s* at ~ 1364 eV ($E_B \approx 123$ eV), Cu-3*p* at ~ 1411 eV ($E_B \approx 75$ eV) and Cu-3*d* at ~1484 eV ($E_B \approx 2$ eV). The peaks occurring at kinetic energies of ~ 720 – 935 eV are due to Cu-*LMM* Auger electrons, resulting from the production of an $L_3$ hole that is filled by an $M_2$, $M_3$, $M_4$, or $M_5$ electron leading to the ejection of an $M_2$, $M_3$, $M_4$, or $M_5$ Auger

ACCEPTED MANUSCRIPT
Journal of Applied Physics
AIP Publishing
This is the author's peer reviewed, accepted manuscript. However, the online version of record will be different from this version once it has been copyedited and typeset.
PLEASE CITE THIS ARTICLE AS DOI: 10.1063/5.0336473

electron. In addition, the O-1*s* line at a kinetic energy of ~ 955 eV ($E_B \approx 531$ eV) and C-1*s* line at ~ 1202 eV ($E_B \approx 285$ eV) were identified. We attribute these to the brief exposure to atmosphere when transferring the sample into the XPS chamber resulting, respectively, in oxidation of the reduced Cu grains and adventitious carbon contamination.

ACCEPTED MANUSCRIPT
Journal of Applied Physics
AIP Publishing
This is the author's peer reviewed, accepted manuscript. However, the online version of record will be different from this version once it has been copyedited and typeset.
PLEASE CITE THIS ARTICLE AS DOI: 10.1063/5.0336473

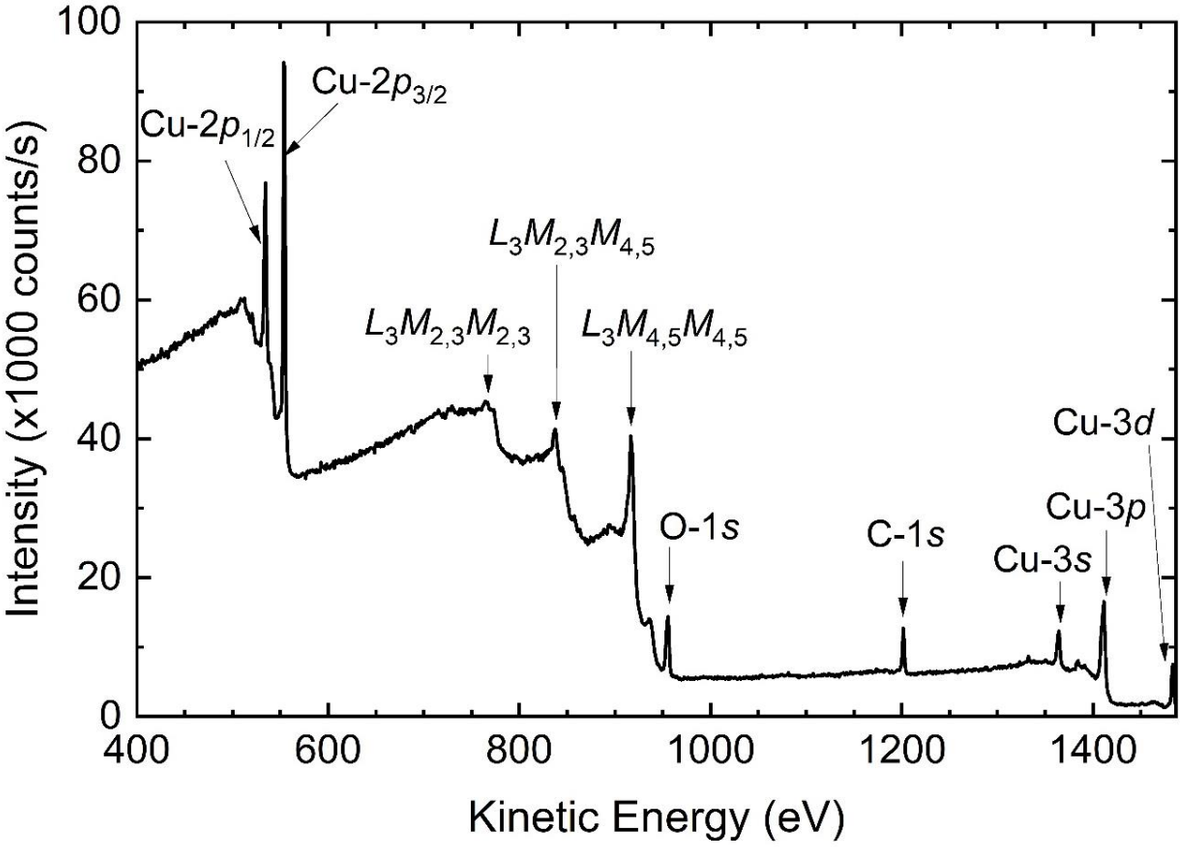



**Fig. 3.** XPS kinetic energy survey spectrum of the reduced Cu grains. The spectrum shows Cu core-level lines and Cu-*LMM* Auger lines, as well as O-1*s* and C-1*s* core-level lines. Electrons originating from deeper below the sample surface lose energy due to inelastic collisions, contributing to the broad background at energies below each of the labeled lines.

ACCEPTED MANUSCRIPT
Journal of Applied Physics
AIP Publishing
This is the author's peer reviewed, accepted manuscript. However, the online version of record will be different from this version once it has been copyedited and typeset.
PLEASE CITE THIS ARTICLE AS DOI: 10.1063/5.0336473

We used the HR XPS spectra of Cu-2*p*, Cu-$L_3M_{4,5}M_{4,5}$, and O-1*s* features for qualitative and quantitative surface analysis of the reduced Cu grains. Figure 4(a) shows the HR Cu-2*p* doublet spectrum, with narrow peaks at 534.3 and 554.1 eV ($E_B$ = 952.3 and 932.5 eV). No shake-up peaks around ~ 520 and 540 eV, characteristic of cupric ($Cu^{2+}$) compounds [30], were observed, suggesting that the reduction treatment effectively removed the oxygen from CuO. However, it was challenging to differentiate metal Cu and cuprous ($Cu^{+}$) compounds ($Cu_2O$) using only the Cu-2*p* spectrum, as their energies differ by only ~ 0.1 eV [34]. Fortunately, their energies are well separated in the Cu-$L_3M_{4,5}M_{4,5}$ spectra. As shown in Fig. 4(b), we observed both metallic Cu at 918.8 eV (peak 0) and $Cu^{+}$ at 916.8 eV (peak 1). These Cu peak positions and assignments were consistent with those reported in the literature [34 – 36]. Platzman et al. [34] investigated the oxidization of Cu films at ambient conditions using the Cu-2*p* and Cu-$L_3M_{4,5}M_{4,5}$ spectra. After the Cu films were exposed to ambient conditions for ~ 1 h, they measured a Cu-to-$Cu^{+}$ intensity ratio of ~1.1 without detectable $Cu^{2+}$. They estimated the thickness of the oxidization layer using the Strohmeier equation [37], and suggested a Cu-to-$Cu^{+}$ ratio of ~ 1.1 corresponded to a surface oxidization layer of ~ 2.5 nm. Fitting the Cu-to-$Cu^{+}$ peak intensity ratios in Fig. 4(b), we find a ratio of ~ 0.98. Thus, we estimated the $Cu_2O$ surface layer was less than ~ 2.5 nm. The HR O-1*s* spectrum in Fig. 4(c) shows O chemical states consistent with $Cu_2O$, hydroxyl ($OH^{-}$) group and $H_2O$ [34], consistent with the above interpretation.

ACCEPTED MANUSCRIPT
Journal of Applied Physics
AIP Publishing
This is the author's peer reviewed, accepted manuscript. However, the online version of record will be different from this version once it has been copyedited and typeset.
PLEASE CITE THIS ARTICLE AS DOI: 10.1063/5.0336473

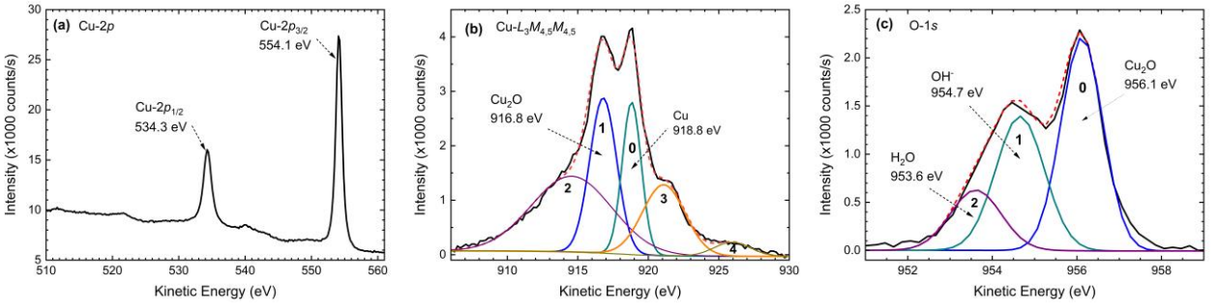



**Fig. 4.** HR XPS spectra for the reduced Cu powder. (a) The Cu-2*p* doublet. (b) Peak fitting of the Cu-$L_3M_{4,5}M_{4,5}$ feature. The peaks at 918.8 eV (peak 0, Cu metal) and 916.8 eV (peak 1, $Cu_2O$) correspond to Cu metal and $Cu_2O$, respectively. The other three peaks are attributed to *LLM* Coster-Kronig-type Auger transitions [38]. (c) Peak fitting of the O-1*s* spectrum showing peaks at 956.1 eV (peak 0, $E_B \approx 530.5$ eV), 954.7 eV (peak 1, $E_B \approx 531.9$ eV), and 953.6 eV (peak 2, $E_B \approx 533.0$ eV). These correspond to $Cu_2O$, hydroxyl group ($OH^-$), and $H_2O$, respectively.

2.4.3 EDS Measurements

ACCEPTED MANUSCRIPT
Journal of Applied Physics
AIP Publishing
This is the author's peer reviewed, accepted manuscript. However, the online version of record will be different from this version once it has been copyedited and typeset.
PLEASE CITE THIS ARTICLE AS DOI: 10.1063/5.0336473

We performed elemental composition analysis using the EDS analysis integrated on the SEM. EDS is sensitive to the composition to a depth determined by the energy of the electrons used. Here we used 10 and 15 keV electrons, resulting in a penetration depth of ~ 450 nm, as estimated with Kanaya-Okayama equation [39]. The results using 10 keV electrons are shown in Fig. 5, indicating that the reduction efficiently removed O and C from the grains and resulted in a 100% metallic Cu within the EDS penetration depth. The EDS analysis also confirms that there was negligible re-oxidization of the grains resulting from the short-period exposure to atmosphere during sample transfer. This analysis was repeated multiple times, on multiple regions. The results were always consistent.

ACCEPTED MANUSCRIPT
Journal of Applied Physics
AIP Publishing
This is the author's peer reviewed, accepted manuscript. However, the online version of record will be different from this version once it has been copyedited and typeset.
PLEASE CITE THIS ARTICLE AS DOI: 10.1063/5.0336473

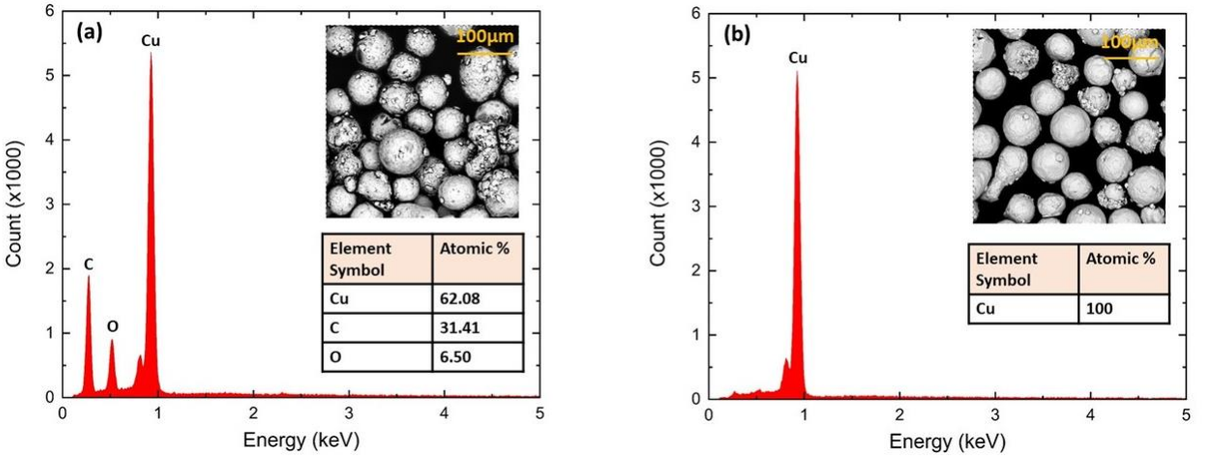



**Fig. 5.** EDS analysis of the Cu grains (a) before and (b) after reduction. The EDS spectra shown were collected using 10 keV primary electrons in backscattered electron mode. The top inset in each panel shows the SEM image of the region where the EDS spectrum was taken. The bottom inset shows the quantitative results of the elemental composition.

ACCEPTED MANUSCRIPT
Journal of Applied Physics
AIP Publishing
This is the author's peer reviewed, accepted manuscript. However, the online version of record will be different from this version once it has been copyedited and typeset.
PLEASE CITE THIS ARTICLE AS DOI: 10.1063/5.0336473

### 2.4.4 XRD Measurements

We characterized the Cu grains using XRD, which is a bulk technique that provides crystalline information of the grains. Figure 6 shows the XRD patterns for both the as-received and reduced grains, collected with a Malvern Panalytical XPERT3 powder diffractometer. Both sample show similar patterns, matching very well with the typical face-centered cubic crystal structure of copper metal with a lattice parameter of 3.6150 Å and an Fm-3m (No. 255) space group [40]. We did not observe any XRD peaks that would be indicative of Cu oxidation states [41]. This confirms that the bulk of each grain was pure polycrystalline Cu. Interestingly, though XRD is not sensitive to localized regions such as the surface of the grains [42], the results in Fig. 6 do suggest that the oxidization state in the as-received grains was located near the surface of the grains. The XRD peaks for the reduced grains systematically shifts by ~ 0.15°, which is likely due to changes in lattice strain when removing the O during reduction [43]. This suggestion of surface oxidation on the as-received grains is consistent with our XPS results.

ACCEPTED MANUSCRIPT
Journal of Applied Physics
AIP Publishing
This is the author's peer reviewed, accepted manuscript. However, the online version of record will be different from this version once it has been copyedited and typeset.
PLEASE CITE THIS ARTICLE AS DOI: 10.1063/5.0336473

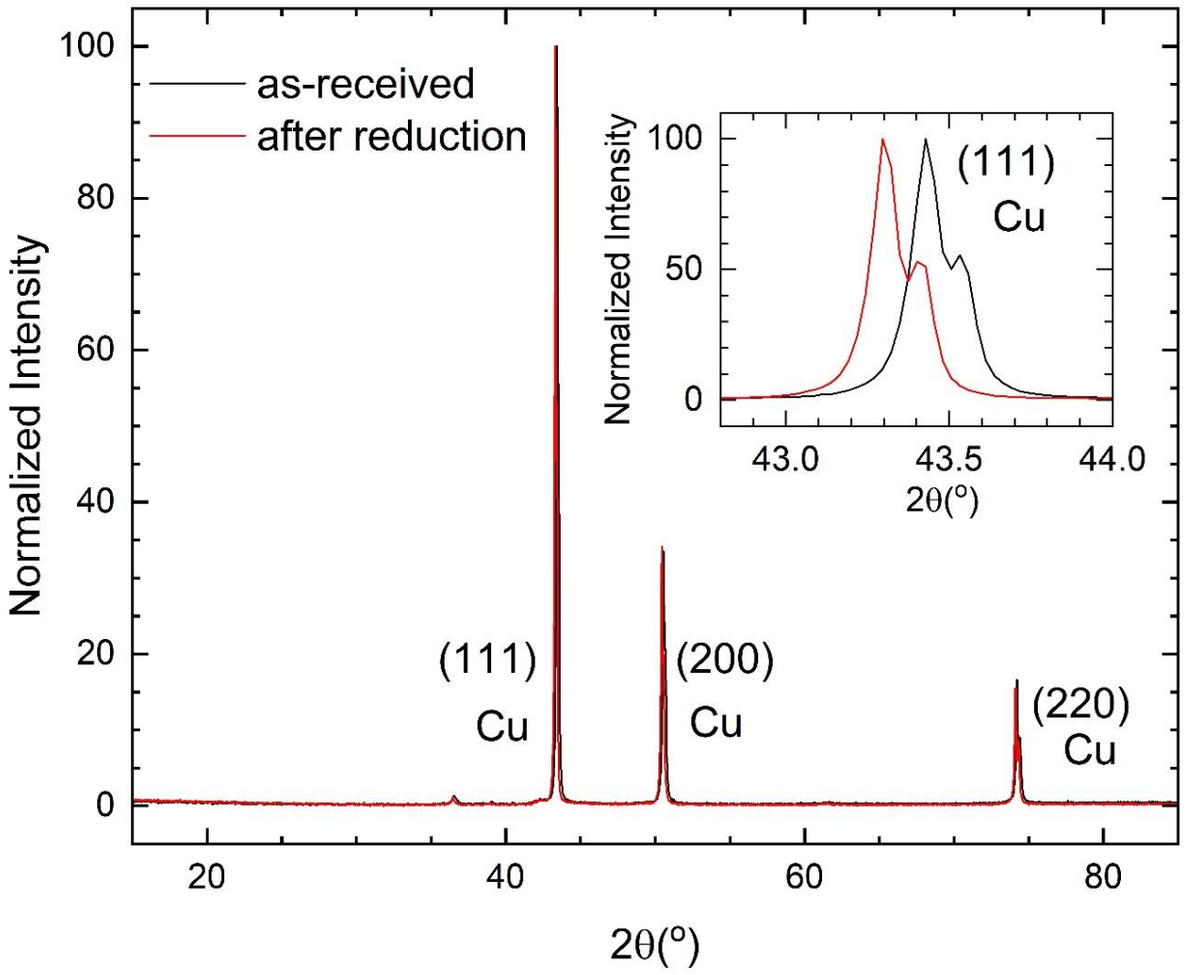



**Fig. 6.** The normalized intensity of scattered X-rays as a function of the diffraction angle (2θ) for the Cu grains as-received (black-line) and after reduction (red-line). Both patterns match well with the XRD peaks for the standard Cu metal [40]. The inset shows that the positions of the XRD patterns for the grains after reduction have systematically shifted to smaller angles by ~ 0.15°. This is likely due to changes in lattice strain when removing the O during reduction [43].

ACCEPTED MANUSCRIPT
Journal of Applied Physics
AIP Publishing
This is the author's peer reviewed, accepted manuscript. However, the online version of record will be different from this version once it has been copyedited and typeset.
PLEASE CITE THIS ARTICLE AS DOI: 10.1063/5.0336473

### 2.5 Sputtering Yields

To derive sputtering yields, the mass of each collector was measured ex-situ using a quartz-crystal microbalance (Mettler Toledo, LLC, Columbus, OH, USA; model: UMX2) integrated into a trace metal clean, automated weighing system [23]. Each collector was weighed in triplicate sequentially before weighing the next collector in triplicate, and so on; any triplicate weighing with an anomalously high standard deviation > 0.3 μg was repeated. This weighing process for every collector was repeated on three separate runs of the auto handler for a total of 9 weights being used to obtain an average pre-mass. The same process was carried out after ion irradiation to obtain the average post-mass of each collector, with the net mass gain being obtained from the difference of the pre- and post- averages. Included within these runs were 4 witness collectors that act as procedural blanks. The average mass change of the 4 witness collectors was subtracted from the net mass gain of each collector to get a final mass gain. The total time between the initial set of weighings of the collectors and the post-experiment set of weighings was 126 days. The final mass gain of each collector was converted into a total number of Cu atoms. The absolute doubly differential sputtering yield at each collector was determined from the number of collected Cu atoms divided by the total ion dose delivered and by the subtended solid angle.

## 3 Theoretical Modeling

A detailed description of our theoretical model is given in Verkercke et al. [22], along with a brief review of related work by other groups. Here we provide only a high level overview of our model and refer the reader to [22] for additional details.

### 3.1 Simulation of the Cu Powder Sample

The Cu powder sample is simulated using the open-source code Large-scale Atomic/Molecular Massively Parallel Simulator (LAMMPS) GRANULAR package [44]. First, a total of 8000 spherical grains with zero initial velocity and a downward acceleration equivalent of 9.81 m $s^{-2}$ (equivalent to Earth's gravity) were dropped into a simulation box. The box had a bottom of 1 mm × 1 mm fixed in the *xy* plane (at $z = 0$), with the height along the +*z* direction. The grains were dropped from a region between $z = 3 – 4.5$ mm. The grain size followed a uniform distribution within diameters of 50 – 90 μm. The grain-on-grain contacts were described by a Johnson–Kendall–Roberts contact model [45]. After all the dropped grains had settled into their final position (forming a height of 4.2 mm), a small force of random direction along the *xy* plane was applied to each grain to "shake" the sample, reducing the sample height to 3.3 mm. Finally, we removed the top 600 μm layer, which consisted of fairy-castle like structures [46, 47], and the bottom 200 μm layer, which was affected by the fixed bottom boundary condition. The final sample height was 2.5 mm with a bulk density of 4.48 g $cm^{-3}$ and a porosity of $p = 0.49$, agreeing closely with the experimental values of $\rho_{powder} = 4.78 \pm 0.24$ g $cm^{-3}$ and $p = 0.46 \pm 0.03$. This excellent agreement between the granular model and the measured values supports our implicit assumption that the Cu grains are free of any significant internal voids.

### 3.2 Ray-tracing Simulation of Kr Ions Impacting the Cu Powder

ACCEPTED MANUSCRIPT
Journal of Applied Physics
AIP Publishing
This is the author's peer reviewed, accepted manuscript. However, the online version of record will be different from this version once it has been copyedited and typeset.
PLEASE CITE THIS ARTICLE AS DOI: 10.1063/5.0336473

Kr atoms (the simulation package considered only neutral impactors) were launched from a plane above the powder target with a global incident polar angle $\theta_i = 45°$ with respect to the bulk surface normal. The initial position of the impactor on the launching plane was selected using a Monte Carlo simulation. Together with the impactor velocity vector, this determined the impact point on the Cu powder sample. An impact occurred if the distance between a Kr atom and a grain was smaller than the radius of the grain. The local normal vector with respect to the grain surface was the vector from the grain center to the impact position, and the local incidence angle, $\theta_i'$, was the angle between the impactor velocity vector and the local normal vector.

In the next step of the simulation, we used SDTrimSP simulations to produce a mapping from $\theta_i'$ to both the yield and its angular distribution. We conducted a series of binary collision approximation (BCA) simulations for 20 keV Kr atoms impacting a flat Cu target for $\theta_{i,k}'$ between 0° and 90° in 5° steps ($k$ = 1 – 20). The simulations were performed using SDTrimSP (Version 7.00) [48] in standard mode with serial processing. SDTrimSP tracks the kinetic energy of the sputtered and substrate atoms but does not consider the effects of atomic ionization, ionic neutralization, potential sputtering, substrate crystallinity, or surface roughness. The resulting double differential sputtering yields versus $\theta_{i,k}'$ were binned in direction in 5° × 5° bins in both polar and azimuthal angles of the ejecta.

To compute the sputtering yield for a particular $\theta_i'$, we approximated each impact as occurring on a flat surface, as the scale of the impact is orders of magnitude smaller than the grain size. Using the resulting value of $\theta_i'$ for a given Kr impactor, the sputtering yield distribution was determined from a linear interpolation of the distribution map for $\theta_{i,k}' \leq \theta_i' \leq \theta_{i,k+1}'$ from SDTrimSP simulations. Based on the resulting distribution, a Monte Carlo sampling was used to determine the local polar, $\theta_s'$, and azimuthal, $\phi_s'$, angles for each ejected atom. The local coordinates of each ejected atom was then transformed to the global coordinates. The trajectory for each ejected atom within the simulated volume was then traced. If an ejected Cu atom crossed the plane from which the impactors were launched, it was considered to have escaped from the powder. If it encountered another grain, it was assumed to stick with a 100% probability, i.e., it was retained within the sample. Finally, we mapped the escaped atoms onto the dome and recorded if they intersected a collector. This enabled us to compare the simulation results with the experimental measurements.

## 4 Results and Discussion

### 4.1 Absolute Doubly Differential Angular Escaping Sputtering Yields

The measured absolute doubly differential angular escaping sputtering yields of the Cu grains are presented in Fig. 7(a). The sputtered mass gains of the collectors have a distribution from a high of 21.17 µg to a low of 0.88 µg, corresponding to a sputtering yield range from 4.598 to 0.19 atoms ion$^{-1}$ sr$^{-1}$. These are the mass gains after subtracting the average mass gain of the four witness collectors, which was 0.72 ± 0.12 µg. We attribute the mass gain of the witness collectors to atmospheric contamination during the ex situ transport and handling of all the collectors. The measured sputtered mass gains ($\Delta m$) are also given in Table 1. The corresponding uncertainties in the mass gain ($\sigma_{\Delta m}$) are given by the quadrature sum of the uncertainty for QCM measurements and the uncertainty in the subtracted average mass gain of the witness collectors. The sputtering yields presented here are calculated assuming a 100% Cu-Cu sticking coefficient and ignoring the

ACCEPTED MANUSCRIPT
Journal of Applied Physics
AIP Publishing
This is the author's peer reviewed, accepted manuscript. However, the online version of record will be different from this version once it has been copyedited and typeset.
PLEASE CITE THIS ARTICLE AS DOI: 10.1063/5.0336473

differences in the Au-Cu sticking coefficient for the first layer of the deposited Cu atoms. As discussed in Bu et al. [23], the energy-distribution-averaged Au-Cu sticking coefficient was (78 ± 4) %. Thus, the 100% assumption here results in an underestimation in the sputtering yield onto any individual collector of 0.014 atoms $ion^{-1}$ $sr^{-1}$.

To evaluate the effects of the small offset between the ion beam center and the target center, we performed SDTrimSP simulations for 20 keV $Kr^+$ incident upon a slab at $\theta_i = 45°$ impacting at target center and impacting ~ 0.3 mm away from the target center. The displacement in incidence plane was in the $\phi_s = 0°$ direction and was 0.03 ± 0.36 mm. The displacement perpendicular to the incident plane was in the $\phi_s = 270°$ direction and was 0.32 ± 0.49 mm. For an average displacement of (0.03, 0.32), the resulting sputtering yield differed by less than ± 3% for each of collectors. To evaluate the effect of the beam size, we shifted the incoming Kr ions to the extreme edges of the beam spot in both the incidence plane and the perpendicular plane. Averaging the SDTrimSP results for these four cases produced sputtering yields on each collector that were within ± 4.5% of those with the impacting point at the sample center. Taking into account these uncertainties and the ~ 10% uncertainty from the BPM measurements, yields an uncertainty of ~ 11%. For the total uncertainty of a given sputtering yield measurement, this 11% needs to be added in quadrature with the uncertainties in the sputtered mass gain measurements. This mass gain measurement uncertainty is < 3% for most of the collectors (61 out of 70) and increases to ~ 10 % for the lowest mass gain collectors (9 out of 70). Clearly, the BPM error is the dominant uncertainty for the majority of our measurements.

ACCEPTED MANUSCRIPT
Journal of Applied Physics
AIP Publishing
This is the author's peer reviewed, accepted manuscript. However, the online version of record will be different from this version once it has been copyedited and typeset.
PLEASE CITE THIS ARTICLE AS DOI: 10.1063/5.0336473

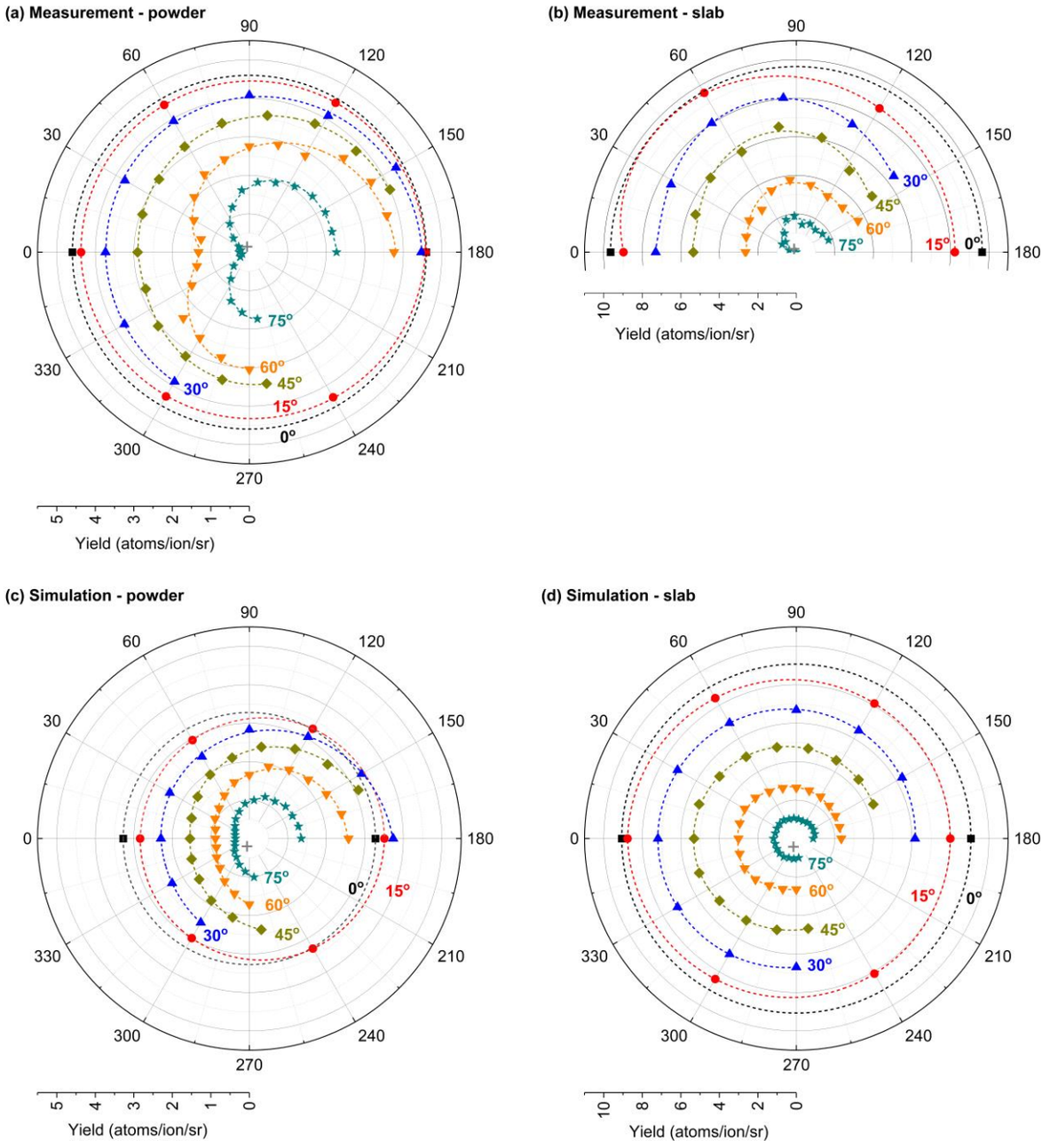



**Fig. 7.** Absolute doubly differential angular escaping sputtering yields as a function of sputtering azimuthal angle $\phi_s$ for sputtering polar angle $\theta_s$ (with respect to the sample normal) of 0° (black square), 15° (red circles), 30° (blue upward triangles), 45° (olive diamonds), 60° (orange downward triangles), and 75° (green stars). The projection of the velocity vector for the impacting 20 keV $Kr^+$ ions is along $\phi_s = 0°$. For $\theta_s = 0°$, there was only one collector. For all other values of $\theta_s$, each data point represents one collector. The dashed lines are polynomial fits to the data. The data in (a) and (b) are our laboratory measurements using Cu powder and slab targets, respectively.

ACCEPTED MANUSCRIPT
Journal of Applied Physics
AIP Publishing
This is the author's peer reviewed, accepted manuscript. However, the online version of record will be different from this version once it has been copyedited and typeset.
PLEASE CITE THIS ARTICLE AS DOI: 10.1063/5.0336473

Panel (b) is reprinted from [23] under a Creative Commons Attribution (CC BY) license (http://creativecommons.org/licenses/by/4.0/). The data in (c) and (d) are results from our simulations using Cu powder and slab targets, respectively.

ACCEPTED MANUSCRIPT
Journal of Applied Physics
AIP Publishing
This is the author's peer reviewed, accepted manuscript. However, the online version of record will be different from this version once it has been copyedited and typeset.
PLEASE CITE THIS ARTICLE AS DOI: 10.1063/5.0336473

560 **Table 1** – Data for Figs. 7(a), 7(c), and 7(d): polar $\theta_s$ and azimuthal $\phi_s$ angles of each collector; together with the measured mass gain $\Delta m$; variance in the measured mass gain $\sigma_{\Delta m}$; and the absolute
562 measured and simulated doubly differential escaping sputtering yields $(dY/d\Omega)_m$ and $(dY/d\Omega)_s$, respectively.

564

| $\theta_s$ | $\phi_s$ | $\Delta m$ | $\sigma_{\Delta m}$ | $(dY/d\Omega)_m$ powder | $(dY/d\Omega)_s$ powder | $(dY/d\Omega)_s$ slab |
|---|---|---|---|---|---|---|
| (degree) | (degree) | (μg) | (μg) | (atoms ion$^{-1}$ sr$^{-1}$) | (atoms ion$^{-1}$ sr$^{-1}$) | (atoms ion$^{-1}$ sr$^{-1}$) |
| 0.0 | 0.00 | 21.17 | 0.16 | 4.594 | 3.275 | 9.068 |
| 15.0 | 0.00 | 20.13 | 0.16 | 4.368 | 2.835 | 8.764 |
| 15.0 | 60.00 | 20.37 | 0.13 | 4.420 | 2.951 | 8.428 |
| 15.0 | 120.00 | 20.65 | 0.16 | 4.481 | 3.295 | 8.108 |
| 15.0 | 180.00 | 21.11 | 0.13 | 4.580 | 3.506 | 7.993 |
| 15.0 | 240.00 | 20.05 | 0.18 | 4.351 | 3.300 | 8.108 |
| 15.0 | 300.00 | 19.95 | 0.13 | 4.328 | 2.989 | 8.428 |
| 30.0 | 0.00 | 17.21 | 0.16 | 3.734 | 2.295 | 7.187 |
| 30.0 | 30.00 | 17.19 | 0.13 | 3.730 | 2.384 | 7.125 |
| 30.0 | 60.00 | 18.14 | 0.15 | 3.935 | 2.459 | 6.936 |
| 30.0 | 90.00 | 18.80 | 0.18 | 4.078 | 2.833 | 6.684 |
| 30.0 | 120.00 | 18.85 | 0.18 | 4.090 | 3.051 | 6.484 |
| 30.0 | 150.00 | 20.26 | 0.17 | 4.397 | 3.367 | 6.342 |
| 30.0 | 180.00 | 20.59 | 0.14 | 4.467 | 3.734 | 6.160 |
| 30.0 | 270.00 | N/A | N/A | N/A | 2.809 | 6.684 |
| 30.0 | 300.00 | 17.90 | 0.18 | 3.884 | 2.522 | 6.936 |
| 30.0 | 330.00 | 17.26 | 0.16 | 3.746 | 2.315 | 7.125 |
| 45.0 | 0.00 | 13.37 | 0.13 | 2.901 | 1.540 | 5.313 |
| 45.0 | 19.50 | 13.57 | 0.15 | 2.943 | 1.590 | 5.355 |
| 45.0 | 39.00 | 13.90 | 0.16 | 3.016 | 1.727 | 5.132 |
| 45.0 | 58.50 | 14.82 | 0.17 | 3.217 | 1.949 | 4.983 |
| 45.0 | 78.00 | 15.78 | 0.14 | 3.424 | 2.148 | 4.849 |
| 45.0 | 97.50 | 16.52 | 0.14 | 3.584 | 2.402 | 4.717 |
| 45.0 | 117.00 | 17.28 | 0.17 | 3.749 | 2.612 | 4.563 |
| 45.0 | 136.50 | 17.61 | 0.16 | 3.821 | 2.799 | 4.454 |
| 45.0 | 156.00 | 18.42 | 0.16 | 3.997 | 3.100 | 4.373 |
| 45.0 | 262.50 | 15.87 | 0.16 | 3.443 | 2.388 | 4.717 |
| 45.0 | 282.00 | 15.61 | 0.15 | 3.387 | 2.094 | 4.849 |
| 45.0 | 301.50 | 14.60 | 0.16 | 3.168 | 1.891 | 4.983 |
| 45.0 | 321.00 | 14.05 | 0.13 | 3.048 | 1.677 | 5.132 |
| 45.0 | 340.50 | 13.15 | 0.17 | 2.854 | 1.590 | 5.355 |
| 60.0 | 0.00 | 6.09 | 0.14 | 1.321 | 0.883 | 3.006 |
| 60.0 | 15.00 | 5.98 | 0.17 | 1.298 | 0.909 | 3.047 |
| 60.0 | 30.00 | 7.66 | 0.15 | 1.662 | 1.028 | 3.100 |
| 60.0 | 45.00 | 9.32 | 0.18 | 2.021 | 1.111 | 3.005 |
| 60.0 | 60.00 | 10.76 | 0.13 | 2.335 | 1.296 | 2.809 |
| 60.0 | 75.00 | 11.51 | 0.13 | 2.497 | 1.513 | 2.719 |

ACCEPTED MANUSCRIPT
Journal of Applied Physics
AIP Publishing
This is the author's peer reviewed, accepted manuscript. However, the online version of record will be different from this version once it has been copyedited and typeset.
PLEASE CITE THIS ARTICLE AS DOI: 10.1063/5.0336473

| | | | | | | |
|---|---|---|---|---|---|---|
| 60.0 | 90.00 | 12.66 | 0.14 | 2.747 | 1.655 | 2.643 |
| 60.0 | 105.00 | 13.32 | 0.13 | 2.890 | 1.931 | 2.588 |
| 60.0 | 120.00 | 13.34 | 0.15 | 2.895 | 2.066 | 2.512 |
| 60.0 | 135.00 | 15.94 | 0.14 | 3.459 | 2.164 | 2.409 |
| 60.0 | 150.00 | 16.84 | 0.15 | 3.653 | 2.310 | 2.350 |
| 60.0 | 165.00 | 17.05 | 0.16 | 3.699 | 2.477 | 2.322 |
| 60.0 | 180.00 | 17.31 | 0.13 | 3.756 | 2.575 | 2.337 |
| 60.0 | 270.00 | 14.05 | 0.16 | 3.049 | 1.710 | 2.643 |
| 60.0 | 285.00 | 13.04 | 0.17 | 2.830 | 1.483 | 2.719 |
| 60.0 | 300.00 | 11.84 | 0.16 | 2.569 | 1.283 | 2.809 |
| 60.0 | 315.00 | 11.17 | 0.15 | 2.424 | 1.081 | 3.005 |
| 60.0 | 330.00 | 7.94 | 0.17 | 1.72 | 0.981 | 3.10 |
| 60.0 | 345.00 | 6.49 | 0.16 | 1.41 | 0.887 | 3.05 |
| 75.0 | 0.00 | 1.22 | 0.15 | 0.265 | 0.360 | 1.19 |
| 75.0 | 13.85 | 1.06 | 0.17 | 0.229 | 0.382 | 1.13 |
| 75.0 | 27.69 | 1.44 | 0.14 | 0.312 | 0.418 | 1.14 |
| 75.0 | 41.54 | 2.52 | 0.13 | 0.547 | 0.496 | 1.15 |
| 75.0 | 55.38 | 4.11 | 0.13 | 0.892 | 0.618 | 1.16 |
| 75.0 | 69.23 | 5.76 | 0.15 | 1.25 | 0.747 | 1.08 |
| 75.0 | 83.08 | 7.48 | 0.16 | 1.62 | 0.911 | 1.07 |
| 75.0 | 96.92 | 8.42 | 0.13 | 1.83 | 1.01 | 1.01 |
| 75.0 | 110.77 | 8.88 | 0.15 | 1.93 | 1.16 | 0.969 |
| 75.0 | 124.62 | 9.56 | 0.14 | 2.07 | 1.17 | 1.01 |
| 75.0 | 138.46 | 10.10 | 0.17 | 2.191 | 1.258 | 1.003 |
| 75.0 | 152.30 | 10.28 | 0.17 | 2.230 | 1.263 | 1.007 |
| 75.0 | 166.15 | 10.20 | 0.16 | 2.213 | 1.315 | 0.982 |
| 75.0 | 180.00 | 10.43 | 0.14 | 2.264 | 1.351 | 0.873 |
| 75.0 | 263.08 | 8.05 | 0.15 | 1.75 | 1.01 | 1.01 |
| 75.0 | 276.92 | 7.26 | 0.17 | 1.58 | 0.865 | 1.07 |
| 75.0 | 290.77 | 6.23 | 0.16 | 1.35 | 0.727 | 1.08 |
| 75.0 | 304.62 | 3.88 | 0.18 | 0.841 | 0.586 | 1.16 |
| 75.0 | 318.46 | 2.50 | 0.17 | 0.543 | 0.511 | 1.15 |
| 75.0 | 332.31 | 1.20 | 0.17 | 0.261 | 0.422 | 1.14 |
| 75.0 | 346.15 | 0.88 | 0.17 | 0.19 | 0.39 | 1.10 |

ACCEPTED MANUSCRIPT
Journal of Applied Physics
AIP Publishing
This is the author's peer reviewed, accepted manuscript. However, the online version of record will be different from this version once it has been copyedited and typeset.
PLEASE CITE THIS ARTICLE AS DOI: 10.1063/5.0336473

### 4.2 Total Escaping Sputtering Yields

To obtain the total escaping sputtering yield, we first interpolated and extrapolated the measured data points to cover $\theta_s = 0 - 90°$ and $\phi_s = 0 - 360°$, both with a step size of 1°. The total experimental yield $Y$ was then calculated by integrating the results over the $\theta_s$-$\phi_s$ plane using:

$$Y = \int_{\theta_s=0^\circ}^{90^\circ} \int_{\phi_s=0^\circ}^{360^\circ} (d\,Y/d\,\Omega) \sin\theta_s \, d\theta_s d\phi_s \qquad \text{Eq. (1)}$$

This gives a total sputtering yield of $Y_E = 15.8 \pm 2.0$ atoms ion$^{-1}$ for the powder measurements in Fig. 7(a). This is the sputtering yield of atoms that escape the powder. Unfortunately, we are not able to determine the sputtering yield for atoms that are retained within the powder. But we can compare our results to our earlier Cu slab measurements. The measured total escaping sputtering yield for the Cu flat slab under similar irradiation conditions was $Y_F = 23.4 \pm 4.7$ atoms ion$^{-1}$ [23]. The resulting powder-to-slab ratio of the measured total sputtering yields is $Y_E/Y_F = 0.675 \pm 0.160$.

It is challenging to compare our total sputtering yield results to most previously published experimental [17, 20, 49] and theoretical [20, 21, 22] results for powders and fuzzy surfaces because of the differences between the present work and these past works. These differences include impactor species, impactor energy, target composition, porosity, and other factors. In this subsection, we have chosen to compare primarily to the ratio $Y_E/Y_F$. This approximately cancels out the effects of impactor species, impactor energy, surface binding energy, and target composition, in attempt to focus on how the granular geometry of a loose powder alters the sputtering yield as compared to fuzzy and flat targets.

We begin by comparing our results directly to the sputtering measurement from the lightly-packed, loosely-sintered powder of glass grains of Hapke and Cassidy [17], but there are a number of issues that complicate the comparison. In [17], they irradiated basaltic glass using a 2 keV $H^+$ beam. They compared the mass loss from their powder sample, with a grain size distribution finer than 37 μm, to the mass loss from a bead of 7 mm in diameter. However, the sputtering yield from a 7 mm diameter bead is likely to be higher than that of a flat surface. The sputtering yield for ions impacting normal to the top of the bead is expected to be equivalent to that of a flat surface. But as the impact position of the ions moves toward the edge of the bead, the local incidence angle increases, and the sputtering yield also increases (e.g., [15]). Thus, the mass loss measured from the bead is likely to have been larger than that from a flat surface and the powder-to-bead ratio of $0.094 \pm 0.009$ is likely to be an underestimate of the powder-to-slab ratio because of the increased denominator value. This may explain a portion of the factor of ~ 7.2 difference between [17] and our results.

Another likely contributing factor is that at the ion energies of [17] primary knock-on sputtering dominates [15]. The ejecta distribution retains some "memory" of the momentum of the impacting ion and the ejecta is predominantly directed further into the powder. This contrasts with the energy that we are working at where secondary knock-on sputtering dominates and the ejecta lobe is an approximately $\cos^{n_s}(\theta_s)$ distribution relative to the local surface normal [23]. Thus, at the energy used here, the eject distribution is pointed out of the powder. As a result, for the results of [17] a higher redeposition fraction (and correspondingly lower mass loss, i.e., reduced numerator) is expected compared to our results, which could further explain a portion of the ~ 7.2 difference.

ACCEPTED MANUSCRIPT
Journal of Applied Physics
AIP Publishing
This is the author's peer reviewed, accepted manuscript. However, the online version of record will be different from this version once it has been copyedited and typeset.
PLEASE CITE THIS ARTICLE AS DOI: 10.1063/5.0336473

What is unlikely to explain the difference is the formation of surface structure. It was pointed out in [18] that at the fluence of ~ $8 \times 10^{20}$ $H^+$ $cm^{-2}$ used in [17], one expects to form a "needle topography" [50] that could cause redeposition of the ejecta. However, as we discuss in Section 4.5, we see the formation of similar conical structures at our fluence of ~ $2.8 \times 10^{18}$ $Kr^+$ $cm^{-2}$. Thus, this is unlikely to explain the difference. Identifying the various contributors to the observed factor of ~ 7.2 difference would benefit from theoretical simulations using the approach of Verkercke et al. [22], but that is beyond the scope of this work.

We also can compare our total escaping sputtering yield to the theoretical results of Cassidy and Johnson [21]. They predicted the total sputtering yield ratio of a regolith ($Y_E$ in our notation [22] and $Y_R$ in [21]) relative to a flat slab ($Y_F$ in both [22] and [21]). However, a number of differences compromise the comparison. First, [21] presents simulations for $\theta_i = 0°$ and our measurements are for $\theta_i = 45°$. The simulations of [22] find that $Y_E/Y_F$ decreases going from $\theta_i = 0°$ to 45° for the Cu power and slab considered here, a point that we return to below. Second is the question of how the sputtering yield depends on $\theta_i$. In [21], they use the approximation $Y_F(\theta_i)/Y_F(0) \approx \cos^{n_i}(\theta_i)$ for $\theta_i \lesssim 80°$ (where $n_i$ is a fitting parameter), but SDTrimSP simulations for 20 keV Kr impacting on a Cu slab find that this approximation overestimates the sputtering yield for $\theta_i \gtrsim 50°$ [22]. It is likely that this results in an overestimate of the sputtering yield from a regolith. Given these limitations, we can still attempt to compare our experimental results of $Y_E/Y_F = 0.675 \pm 0.160$ to the predictions of [21] for a cosine emission law and a sticking coefficient of $S = 1$, parameters that have been shown to be appropriate for 20 keV $Kr^+$ impacting a Cu slab [23]. Using the data given by [21] in their Table 3, they find $Y_E/Y_F = 0.45$ for $n_i = 1.0$ and 0.64 for $n_i = 1.6$. Using SDTrimSP simulations 20 keV $Kr^+$ impacting a Cu slab [22], for $\theta_i \lesssim 50°$, we find $n_i = 1.4$. Thus we expect that had the simulations of [21] been carried out for $n_i = 1.4$, they would have found $Y_E/Y_F \sim 0.58$ for $\theta_i = 0°$. Based on the simulations of [22], this ratio would be even lower for $\theta_i = 45°$. Thus, it appears that the model of Cassidy and Johnson is likely to under-predict $Y_E/Y_F$. We attribute this to the over-simplification of their model.

Since the work of [21], the only other theoretical simulations we are aware of for ion sputtering from a loose powder are those of Brötzner et al. [20] and our work in Verkercek et al. [22]. In [20], they simulated ion sputtering by 1 keV $H^+$ and 4 keV $He^+$ impacting a lunar regolith sample with a porosity of $p = 0.8$, using a theoretical model that they had scaled to best match their laboratory measurements on a thin film prepared by pulsed laser deposition from the lunar sample. Their model predicts a ratio of $Y_E/Y_F \sim 0.50$ for their regolith sample for both impactors at $\theta_i = 45°$. However, the authors do not explicitly give an accuracy for their scaled model. Here, we have attempted to estimate the accuracy from a comparison of their rough surface model to their measurements. For the rough surface, they used a pressed pellet formed from the regolith sample. At $\theta_i = 45°$, the rough surface measurements for both impactors had error bars of ~ ±30% and the model agreed with the measurements to within these error bars. Thus, our $Y_E/Y_F = 0.675 \pm 0.160$ for $p = 0.46$ and their $Y_E/Y_F \sim 0.50 \pm 0.15$ for $p = 0.8$ agree to within their mutual error bars. However, we note that [22] predicts that the $Y_E/Y_F$ ratio should decrease with increasing porosity. Our results and those of [20], taken together, are suggestive of this prediction; but it is clear that future studies with reduced uncertainties are needed to test this prediction.

ACCEPTED MANUSCRIPT
Journal of Applied Physics
AIP Publishing
This is the author's peer reviewed, accepted manuscript. However, the online version of record will be different from this version once it has been copyedited and typeset.
PLEASE CITE THIS ARTICLE AS DOI: 10.1063/5.0336473

The theoretical simulations that we can most directly compare to are our simulations [22], which is briefly described in Section 3 and applied to our experimental conditions here. That model predicts a total escaping sputtering yield of 10.5 atoms ion$^{-1}$, as calculated with Eq. (1) using the coarse angular binning data in Fig. 7(c). This value is close to the value of 10.6 atoms ions$^{-1}$ output directly by the simulation, with a finer angular binning, indicating that the approximation of Eq. (1) is accurate to within 1%. The ratio of the theoretical-to-experimental values for $Y_E$ is 0.664 ± 0.084. This suggests that either the simulations underestimate the sputtering yield or the experimental values have been enhanced by a process not accounted for in the simulations. We favor the latter explanation. Ion sputtering erodes the exposed surfaces of the grains, thereby reducing the peak heights of the topmost layer of the grains. This correspondingly reduces the shadowing of the ejecta, thereby increasing the escaping sputtering yield in the experiment. This has not been accounted for in the simulations. We discuss this in more detail in Section 4.5.

We can also compare the predicted ratio of $Y_E/Y_F = 0.51$ to our measured value 0.675 ± 0.160. Though these agree to within the one-sigma experimental error bar, the measured ratio is likely affected by the differing levels of surface modification in the experimental results for the powder compared to the slab. We expect the measured $Y_E$ to be affected by any reduction in shadowing due to ion erosion of the topmost grains, as discussed above. No such effect was seen in the comparison of our measured and simulated slab results for $Y_F$ [22, 23]. This is also discussed in more detail in Section 4.5.

Lastly, we compare our powder results for $Y_E/Y_F$ to the fuzzy surface results of Stadlmayr et al. [49]. In [49], they measured the total sputtering yields for He-induced nanostructured tungsten (so-called W fuzz) and a flat W thin film, both impacted by 2 keV $Ar^+$ at $\theta_i = 60°$. From their measurements, they estimated $Y_E/Y_F = 0.059 \pm 0.035$. This is comparable to the ratio of ~ 0.1 reported by Nishijima et al. [51] for their primarily $Ar^+$ plasma sputtering a W fuzz and a flat surface at impactor energies of 50 – 110 eV. These ratios are, respectively, factors of 11.4 ± 7.4 and ~ 7 smaller than our result here. These suggest that sputtering from a noble gas impacting an elementally pure metallic granular target is significantly different from a noble gas impacting an elementally pure metallic fuzz, independent of the ion energy.

Going into more detail in the comparison, we largely limit our discussion to [49], as it is more directly comparable to our study here than that of [51]. The factor of 11.4 ± 7.4 reduction between the results of [49] and ours is unlikely due to the difference in the ion energy or incident angle. Both their work and ours involves a noble gas ion impacting a transition metal; our simulation in [22] indicate that changing the impact angle from 45° to 60° and decreasing the ion energy from 20 to 1 keV, lead to only a factor of $\lesssim 1.3$ reduction in the $Y_E/Y_F$ ratio. We hypothesize that part of the observed difference is due to the structural differences between the Cu powder used here and the W fuzz of [49]. The Cu powder consists of interconnected voids and solid spherical Cu grains. However, SEM images of the W fuzz in [49] show it to be foam-like, comprised of ~ 40 nm thick tendrils. From areal density of SEM images in [49], they estimate a porosity of $p \sim 0.5$; but other groups have measured the porosity of W fuzz to be $p \gtrsim 0.9$ [51, 52] with the tendrils containing He bubbles on the nanometer scale [51 – 54] that cannot be imaged by the SEM method in [49]. This suggests that the tendrils are comprised ~ 80% by voids. Assuming that the walls of the voids in the tendrils are on the nanometer scale, then a sizeable fraction of the incident 2 keV $Ar^+$ ions, with their ~ 2 – 3 nm penetration depth, will pass through the walls and produce sputtering inside

ACCEPTED MANUSCRIPT
Journal of Applied Physics
AIP Publishing
This is the author's peer reviewed, accepted manuscript. However, the online version of record will be different from this version once it has been copyedited and typeset.
PLEASE CITE THIS ARTICLE AS DOI: 10.1063/5.0336473

the voids that is unable to escape the bubbles. This will reduce the escaping sputtering yield of the fuzz through a process that does not occur in a granular target of solid particles. Other differences that need to be considered are that for the powder the granular roughness is on the ~ 50–90 μm scale and the ion-induced surface roughness on the order of ~ 10 μm (see Section 4.5), whereas for the fuzz the surface roughness is on scales < 40 nm. Clearly, future systematic experimental and theoretical studies are needed for granular and foam-like targets and as a function of porosity in order to better understand how these properties control the escaping sputtering yield.

Moving on to rough surfaces of films and pressed pellets [19, 20, 55], a comparison of the integral sputtering yield ratio $Y_E/Y_F$ masks over difference in the underlying differential sputtering process that arise from the lack of porosity in those works. For this reason, we defer to the next section the comparison of our results to those of non-porous rough surfaces of films and pressed pellets.

### 4.3 Escaping Sputtering Yields in the Incidence Plane

The experimental and theoretical differential escaping sputtering yields in the incidence plane, as a function of $\theta_s$, are shown in Fig. 8. The angular distribution for the Cu slab is nearly normal to the surface, being tilted only slightly in the forward direction. This is close to what is expected when the sputtering process is dominated by secondary knock-on collisions [56, 57]. For the Cu powder, the data clearly shows that the ejecta lobe is tilted in the backward direction, which was not observed in previous studies using slabs [56 – 60]. However, qualitatively similar backward-directed ejecta was observed for sputtering of W fuzz by 2 keV $Ar^+$ at $\theta_i = 60°$ [49].

ACCEPTED MANUSCRIPT
Journal of Applied Physics
AIP Publishing
This is the author's peer reviewed, accepted manuscript. However, the online version of record will be different from this version once it has been copyedited and typeset.
PLEASE CITE THIS ARTICLE AS DOI: 10.1063/5.0336473

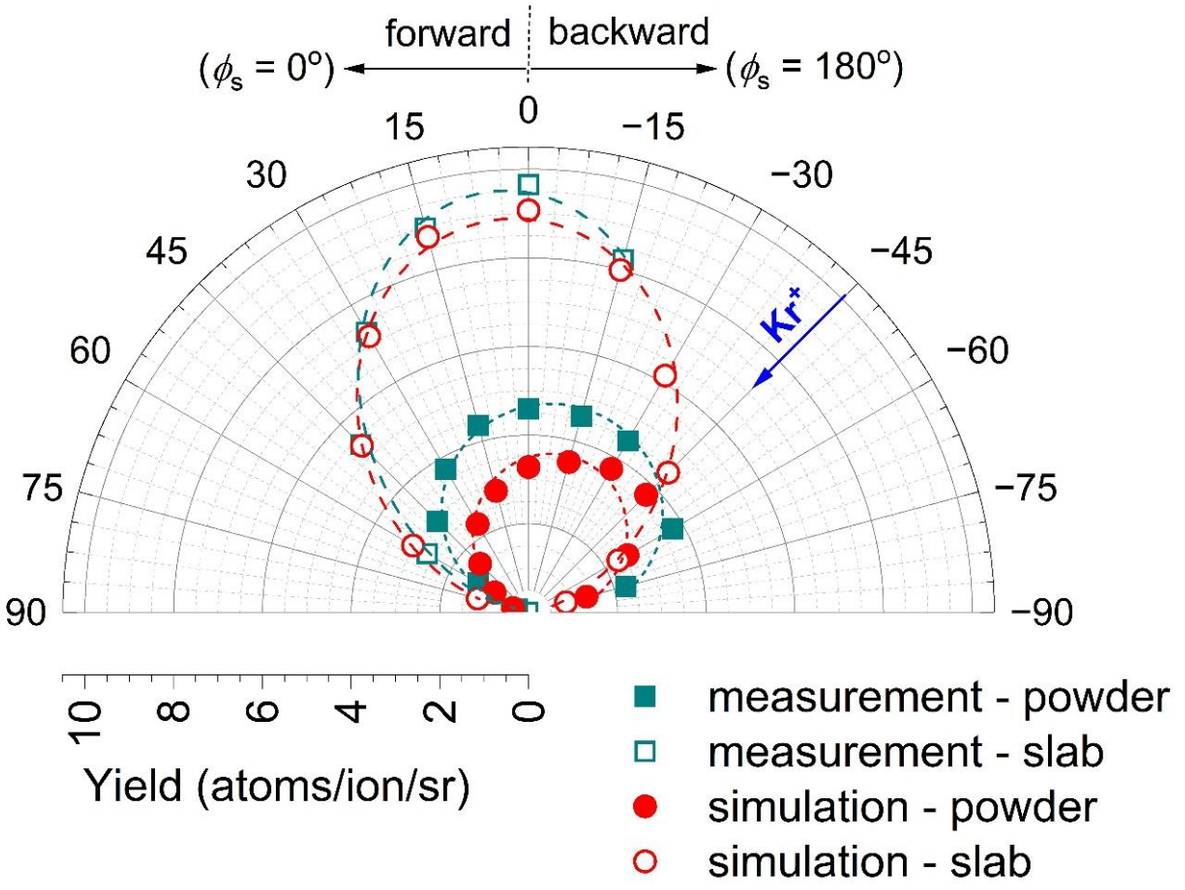



**Fig. 8.** Differential escaping sputtering yields in the incidence plane, as a function of the sputtering polar angle $\theta_s$ (in degrees). The measured yields for the Cu powder and slab are from Figs. 7(a) and 7(b), respectively, while the simulation yields are from Figs. 7(c) and 7(d), respectively. The blue arrow indicates the velocity vector of the 20 keV $Kr^+$ ions. Positive $\theta_s$ is in the forward direction with respect to the velocity vector of the impactor and negative $\theta_s$ is in the backward direction. The dashed lines represent the best fit of the function $A\cos^{n_s}(\theta_s - \gamma)$ to the data points. The powder results are clearly predominantly in the backward direction, as contrasts with the slab results that are nearly normal to the surface, being tilted only slightly in the forward direction. See text for more details.

ACCEPTED MANUSCRIPT
Journal of Applied Physics
AIP Publishing
This is the author's peer reviewed, accepted manuscript. However, the online version of record will be different from this version once it has been copyedited and typeset.
PLEASE CITE THIS ARTICLE AS DOI: 10.1063/5.0336473

736 **Table 2** – The fitting results for the escaping sputtering yields in the incidence plane in Fig. 8, using $A\cos^{n_s}(\theta_s - \gamma)$.

738

| | $A$ | $\gamma$ | $n_s$ |
|---|---|---|---|
| Measured - powder | 4.76 ± 0.12 | –13.2 ± 1.2 | 0.87 ± 0.08 |
| Measured - slab | 9.53 ± 0.27 | 4.3 ± 2.3 | 2.35 ± 0.35 |
| Simulation - powder | 3.64 ± 0.18 | –15.0 ± 2.6 | 1.15 ± 0.18 |
| Simulation - slab | 8.89 ± 0.12 | 3.1 ± 0.6 | 1.75 ± 0.06 |

ACCEPTED MANUSCRIPT
Journal of Applied Physics
AIP Publishing
This is the author's peer reviewed, accepted manuscript. However, the online version of record will be different from this version once it has been copyedited and typeset.
PLEASE CITE THIS ARTICLE AS DOI: 10.1063/5.0336473

We can quantify the tilt of the ejecta lobe using the fitting function $A\cos^{n_s}(\theta_s - \gamma)$, similar to what was done in [19]. Here, $A$, $n_s$, and $\gamma$ are fitting parameters, with $\gamma$ being the tilt angle of the ejecta lobe. The best fit parameters and their $1\sigma$ uncertainties are given in Table 2. Considering the 15° step size in the polar angle of our measurements, we find reasonable agreement between the experimental and theoretical results. For our slab results, we find $\gamma$ = 4.3° ± 2.3° for the measurement and 3.1° ± 0.6° for the simulations, in excellent agreement. For the energy used here, secondary knock-on sputtering dominates, and the ejecta lobe from the slab is expected to be oriented normal to the surface with $\gamma$ = 0°. The slightly positive $\gamma$ suggests a small degree of primarily knock-on sputtering, where the ejected atoms retain memory of the momentum of the incident ions [57, 61]. For the powder, we find $\gamma$ = −13.2° ± 1.2° for the measurements and −15.0° ± 2.6° for the theoretical simulations. Here, the negative sign signifies that the lobe points in the backward direction. That the escaping sputtering yield from the powder is so clearly backward directed we attribute to two differing forms of shadowing by the granular structure of the powder, as we noted in [22]. First, ions can penetrate through the interconnected voids of the powder and cause sputtering from underlying grains. Atoms sputtered from these underlying grains are most likely to escape from the powder if they are ejected roughly in the backward direction toward the origin of the incident ions, while ejecta in other directions are more likely to be shadowed by neighboring grains. Second, for $\theta_i$ = 45°, the ion-irradiated surfaces are primarily oriented in the backward direction, leading to shadowing of the ejecta emitted in the forward direction.

We can compare our tilt angle results to those of Stadlmayr et al. [49] for 2 keV $Ar^+$ impacting their W flat and fuzz targets at $\theta_i$ = 60°. They measured $\gamma \sim 30°$ for the flat target, which is not surprising given the low ion beam energy where primary knock-on collisions dominate. For the fuzz, they measured $\gamma \sim -45°$. Although the ion energy is still in the primary knock-on regime, the structure of the fuzz clearly alters the ejecta distribution. In [22], we showed that $\gamma$ of the ejecta from a powder becomes more negative as $\theta_i$ increases. We attribute the larger degree of backward-directed ejecta for the fuzz compared to that of our powder, in part, to the larger $\theta_i$ in [49] compare to our work here.

Fitting $n_s$ for the slab, we find $n_s$ = 2.35 ± 0.35 for the measurements and 1.75 ± 0.06 for the simulations. These values are significantly larger than 1, indicating an over-cosine angular distribution. This is predicted theoretically to result from the dominance of secondary knock-on sputtering at sufficiently impact high energies [57, 58]. For the powder, we find $n_s$ = 0.87 ± 0.08 for the measurements and 1.15 ± 0.18 for the simulations. Both values are very close to 1, suggesting a nearly cosine angular distribution. We attribute the difference in the angular distributions as being due to a flat versus a granular target. An ideal flat surface has a single normal vector across the surface. When secondary knock-on collisions dominate the sputtering process, the ejecta lobe is oriented along this normal vector with an over-cosine independent of $\theta_i$. The angular distribution averaged over the area of the ion beam remains over-cosine. Conversely, for the granular surface, there is a distribution of local surface normal vectors relative to the bulk surface normal vector. At the impact energy considered here, the ejecta lobe at each impact point is oriented along the local surface normal and remains over-cosine. However, when averaged over the distribution of local surface normal vectors spanned by the area of the incident ion beam, the ejecta distribution becomes closer to cosine. Other factors, such as structural defects [59] and ion-irradiation-induced surface roughness [60, 61], may also modify the value of $n_s$. It is clear that

ACCEPTED MANUSCRIPT
Journal of Applied Physics
AIP Publishing
This is the author's peer reviewed, accepted manuscript. However, the online version of record will be different from this version once it has been copyedited and typeset.
PLEASE CITE THIS ARTICLE AS DOI: 10.1063/5.0336473

much future work remains to understand the dependence of $n_s$ with surface structure, but those studies are beyond the scope of this work.

We can also quantify the ratio of the theoretical-to-experimental differential escaping sputtering yields for our powder results. Taking the average of the 10 pairs of data points in Fig. 8 gives a ratio of 0.74 ± 0.23. Taking the ratio of the fitted $A$ values gives 0.76 ± 0.04. These values are consistent with the ratio of 0.664 ± 0.084 for the theoretical-to-experimental values for $Y_E$ given in Section 4.2. That these ratios are less than 1 we attribute to the modification of the powder surface during ion irradiation, as discussed above and further discussed in Section 4.5.

In [22], we have predicted that the opposition effect [62] will create a "surge" in the ejecta for a small cone around $|\theta_s - \theta_i| \lesssim 5°$. This is a direct result of the interconnected voids within the powder, which make the ion beam origin a preferred direction for the ejecta to escape the powder. The opposition effect in the simulations plotted in Fig. 8 is not as obvious as shown in [22], due to the factor of ~ 2 – 3 times larger angular binning resolution dictated by our collector dimensions. Still, the opposition effect can be seen in the simulations for $\theta_i = 45°$, which is the only theoretical value that falls outside the fitted ejecta lobe. Interestingly, no such opposition effect is predicted for W fuzz in the simulations of [49]. We attribute this to the predominantly foam-like nature of the fuzz and correspondingly reduced abundance of interconnected voids that make the ion beam origin a preferred direction.

Experimentally, it is not currently possible to detect the opposition effect. As shown in Fig. 1(b), an opening at $\theta_i = \theta_s = 45°$ on the dome was necessary for the ion beam to reach the target. This opening covered a polar range of $\Delta\theta_s = 20.2°$ and an azimuthal range of $\Delta\phi_s = 28.3°$, impeding the measurement of the opposition effect. Considering the experimental challenges of mounting a detector within a 5° cone of the ion beam, it is unlikely that laboratory studies will be able to detect the opposition effect in the near future.

In addition, we can compare our measured powder results to recent experimental results for rough surfaces and pressed pellets [19, 55, 63]. Cupak et al. [55] measured the sputtering yields in the incidence plane for 2 keV $Ar^+$ at $\theta_i = 60°$ impacting tungsten films of different surface roughness. They characterized their surfaces by the root-mean-square (RMS) surface roughness and the mean value of the surface inclination angle distribution ($\delta_m$). They report results for three surfaces (S1, S2, and S3) where (RMS, $\delta_m$) varied from S1 ≈ (1.7 nm, 7.6°) to S2 ≈ (110 nm, 15.5°), and S3 ≈ (1551 nm, 36.5°). As the surface roughness increased, the tilt in the measured ejecta lobe evolved from $\gamma \sim 30°$ for S1 to $\gamma \sim -5°$ for S3. They attribute this evolution to the increase in $\delta_m$. Biber et al. [19] measured the incident plane sputtering yields by 2 keV $Ar^+$ at $\theta_i = 45°$ impacting thin films and pressed pellets of wollastonite and enstatite. The measured $\delta_m$ for the wollastonite film and pellet were nearly identical and no difference was seen in the reported tilt angles. For the enstatite, they report that the tilt angle $\gamma$ evolves toward bulk surface normal, going from $\gamma = 27° – 34°$ for the thin film ($\delta_m \approx 10°$) to $\gamma = 21° – 25°$ for the pressed pellet ($\delta_m \approx 36°$). Interestingly, their enstatite pressed pellet results for $\delta_m \approx 36°$ are forward directed whereas the S3 tungsten results of [55] for $\delta_m \approx 36°$ are slightly backward directed, despite both targets have RMS values on the μm scale. The reason for these differences is unclear. Most recently, Brötzner et al. [63] measured the incidence plane sputtering yield from 4 keV $He^+$ at $\theta_i = 60°$ impacting a thin film ($\delta_m \approx 6°$) prepared by pulsed laser deposition from a lunar soil and a pressed pellet ($\delta_m \approx 28°$) of

ACCEPTED MANUSCRIPT
Journal of Applied Physics
AIP Publishing
This is the author's peer reviewed, accepted manuscript. However, the online version of record will be different from this version once it has been copyedited and typeset.
PLEASE CITE THIS ARTICLE AS DOI: 10.1063/5.0336473

the same soil. They found that the tilt angle evolved toward the bulk surface normal with increasing $\delta_m$, going from $\gamma \sim 35°$ to $\sim 20°$.

We suggest that a consistent picture is forming for how the ejecta lobe tilt varies with surface roughness and porosity. In [19, 55, 63], the ion beam energies were in the regime where the sputtering was dominated by primary knock-on collisions. They found that $\gamma$ evolved from forward direct toward the bulk surface normal as $\delta_m$ increased. The work of [49] was also in the primary knock-on regime and founds that the ejecta was in the forward direction for a flat surface but strongly in the backward direction for fuzz. Our slab [23] and powder studies are in the secondary knock-on collision regime. We find that the ejecta lobe is nearly normal for a slab but is strongly in the backward direction for the powder. Taken all together, these findings suggest that increasing $\delta_m$ results in an ejecta lobe orientation that evolves toward the bulk surface normal for impact energies where primary knock-on collisions are important, whereas porous surfaces results in strongly backward directed ejecta for impact energies for both primary and secondary knock-on regimes. Clearly, additional studies are needed to investigate this picture; but the findings suggest that rough surfaces with their lack of interconnected porosity are poor analogues for ion sputtering of porous surfaces.

### 4.4 Doubly Differential Angular Escaping Sputtering Yields

Our doubly differential results further demonstrate that for ion sputtering from a powder the ejecta lobe is backward directed. Furthermore, the lobe is not cylindrically symmetric around any axis. Figures 7 and 8 demonstrate that the ejecta lobe is not cylindrically symmetric around the bulk surface normal. Other axes of cylindrical symmetry can also be ruled out; for any given $\theta_s \geq 15°$, the azimuthal distribution shown in Fig. 7 does not exhibit the ellipsoidal shape that would be expected for a conic section of a cylindrically symmetric ejecta lobe.

Returning to the laboratory coordinates, Figs. 7(a) and (c) demonstrate that the escaping sputtering yield increases as $\phi_s$ rotates from the forward direction ($\phi_s = 0°$) to the backward direction ($\phi_s = 180°$), with a peak yield in the backward direction for all $\theta_s > 0°$. The corresponding reduction in the forward direction is most pronounced for the polar angles of $\theta_s = 60°$ and 75°. The measurements show a greater reduction as compared to the simulations. We attribute this, in part, to shadowing due to ion-induced surface roughness of the grains for these large polar angles. A similar shadowing effect was noted in our earlier slab results at these polar angles [23]

We can further quantify the comparison of our powder-to-slab doubly-differential results, as shown in Fig. 9 for both the measurements and the simulations. In general, the ratio is almost always < 1, which is as expected given that the $Y_E/Y_F$ for the total sputtering yields is < 1. Only for combined large $\theta_s$ and $\phi_s$ does the ratio exceed 1. In addition, both panels show qualitatively similar behavior for the increase in the powder-to-slab ratio versus $\phi_s$, which provides partial validation of the simulations. The increase is most similar for $\theta_s = 15°$, 30°, and 45°. The behavior is less similar for $\theta_s = 60°$ and 75°, which we attribute to the formation of ion-induced surface roughness.

ACCEPTED MANUSCRIPT
Journal of Applied Physics
AIP Publishing
This is the author's peer reviewed, accepted manuscript. However, the online version of record will be different from this version once it has been copyedited and typeset.
PLEASE CITE THIS ARTICLE AS DOI: 10.1063/5.0336473

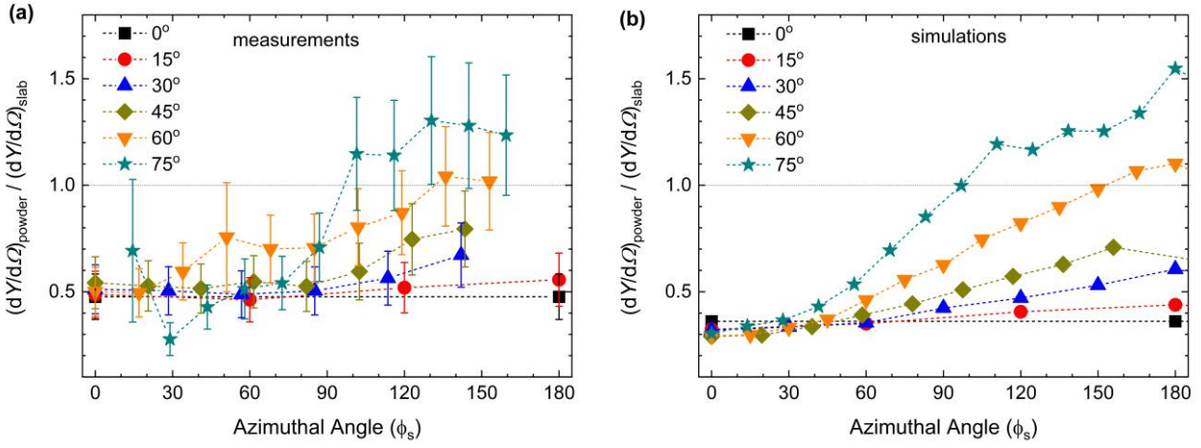



**Fig. 9.** The powder-to-slab ratios of the doubly differential angular escaping sputtering yields as a function of the sputtering azimuthal angles $\phi_s$ for various sputtering polar angles $\theta_s$ for our (a) measurements and (b) simulations. The measurement results are from Figs. 7(a) and 7(b). The error bars represent the quadrature sum of the total experimental uncertainty for the power and slab results. The measurements in Fig. 7(b) were interpolated to match the corresponding $\phi_s$ for the measurements in Fig. 7(a). For $\theta_s = 0°$, we had only one collector, spanning $\phi_s$ between 0° and 360°. For $\theta_s = 75°$ at $\phi_s = 0°$, the measured sputtering yield from Cu slab was consistent with zero, yielding a meaningless ratio that was not included in the plot. The simulations in (b) are from Figs. 7(c) and 7(d). To compare with the measurements, Fig 9(b) only presents azimuthal angles of 0° – 180°.

ACCEPTED MANUSCRIPT
Journal of Applied Physics
AIP Publishing
This is the author's peer reviewed, accepted manuscript. However, the online version of record will be different from this version once it has been copyedited and typeset.
PLEASE CITE THIS ARTICLE AS DOI: 10.1063/5.0336473

The directionality of the yield can also be quantified by the ratio of the backward-to-forward escaping atoms [22] using the data in Fig. 7 and Table 1. Here, we define this quantity as

$$R = \frac{\int_{\theta_S=0^\circ}^{90^\circ}\int_{\phi_S=0^\circ}^{90^\circ}(dY/d\Omega)\sin\theta_S d\theta_S d\phi_S}{\int_{\theta_S=0^\circ}^{90^\circ}\int_{\phi_S=90^\circ}^{180^\circ}(dY/d\Omega)\sin\theta_S d\theta_S d\phi_S}, \quad \text{Eq. (2)}$$

where we do not consider the region of $180° < \phi_s < 360°$ because of the absence of experimental data for much of that range. This definition implicitly assumes mirror symmetry through the incident plane (which we demonstrate later in this subsection). To calculate the above integrals, for those regions without collectors at a given polar angle, we extrapolated from the measurement at that same polar angle. We then use the measured and extrapolated data points and through a combination of interpolation and extrapolation covered $\theta_s = 0 – 90°$ and $\phi_s = 0 – 180°$, both with a step size of 1°. For the measurements, we find $R = 1.41 \pm 0.04$ for the powder and $R = 1.00 \pm 0.06$ for the slab. The uncertainties quoted here are due solely to the uncertainties in the mass gain measurements. For the simulations, we find $R = 1.56$ for the powder and 0.92 for the slab. For the powder, both the measurements and simulations show that the escaping sputtering is enhanced in the backward direction. For the slab, both the measurements and simulations are consistent with a slight enhancement in the forward direction. We attribute the differences between the measurements and simulations to the effects of ion-induced surface modification, which has not been accounted for in the simulations. For the powder results, an additional contribution to the differences in $R$ is that we were unable to measure the opposition effect, while the simulation was able to include it.

We have also explored the mirror symmetry through the incidence plane of the escaping atoms using the data in Fig. 7 and Table 1. We define right as being $0° \leq \phi_s < 180°$ and left as being $180° \leq \phi_s < 360°$. Figure 10(a) shows the ratio $M = (dY_L/d\Omega)/(dY_R/d\Omega)$ for the powder for mirror pairs of $(\theta_s, \phi_s) = (\theta_s, 360° – \phi_s)$. Most of the ratios are scattered close to 1, the value expected for mirror symmetry, though the ratios for $\theta_s = 60°$ are systematically ~ 10% below 1. The uncertainties quoted here are due solely to the uncertainties in the mass gain measurements. To reduce the effects of the scatter, for each given $\theta_s$ we have averaged $M$ over $\phi_s$, which we plot in Fig. 10(b). For $\theta_s =$ 15°, 30°, and 45°, the ratios are $1.03 \pm 0.01$, $1.01 \pm 0.01$, and $1.02 \pm 0.01$, respectively. For $\theta_s =$ 60° it is $0.90 \pm 0.02$ and for $\theta_s = 75°$ it is $1.07 \pm 0.03$. The remaining discrepancies with 1 we attribute to a combination of any potential offset between the beam center and the target center, which is estimated from simulations to increase $M$ by less than 3%; randomness in the granular roughness; and ion-induced surface modification. For the simulated powder, we find ratios of ~ 0.99 – 1.02, which we attribute to randomness introduced by the modeled granular roughness. This is supported by the simulated slab results, for which we found a ratio of 1.00.

ACCEPTED MANUSCRIPT
Journal of Applied Physics
AIP Publishing
This is the author's peer reviewed, accepted manuscript. However, the online version of record will be different from this version once it has been copyedited and typeset.
PLEASE CITE THIS ARTICLE AS DOI: 10.1063/5.0336473

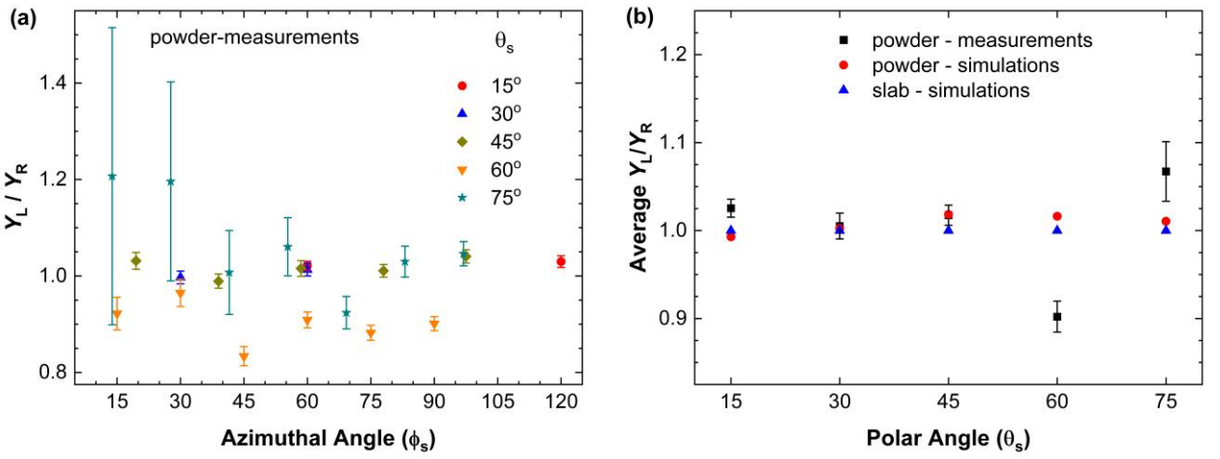



**Fig. 10.** (a) Left-to-right mirror ratio $M = (dY_L/d\Omega)/(dY_R/d\Omega)$ for the Cu powder measurements shown in Fig. 7(a), as functions of polar angle ($\theta_s$) and azimuthal angle ($\phi_s$). (b) The $M$ ratios, averaged over $\phi_s$, as a function of $\theta_s$, for the Cu powder measurements in Fig. 7(a) (black-square with error bars), the Cu power simulations in Fig. 7(c) (red-circles), and the Cu slab simulations in Fig. 7(d) (blue-triangles).

ACCEPTED MANUSCRIPT
Journal of Applied Physics
AIP Publishing
This is the author's peer reviewed, accepted manuscript. However, the online version of record will be different from this version once it has been copyedited and typeset.
PLEASE CITE THIS ARTICLE AS DOI: 10.1063/5.0336473

### 4.5 Effects of Ion-Induced Surface Modification

Multiple previous studies have shown that ion irradiation at incidence angles of ~ 30° – 75° can create various topographies, such as pits, blisters, cones, ripples, needles, and facets [e.g., 23, 52 – 55, 64 – 68]. It is challenging to study these modifications on a loose powder target. We have yet to identify a method to preserve the sample surface and grain orientation for ex situ studies of the modified surface. Removing the sample from the target chamber and transporting it will jostle the grains. Using glue to solidify the sample before removal will introduce flows that can reorient the grains. Here, we have used a transfer process that approximately preserves the orientation of the grains. Using adhesive tape, we gently laid it across a portion of the uppermost layer of grains. The top of the grains adhered to the tape, exposing the bottom of the grains. We next used a second adhesive tape to pick up these grains from their now-exposed bottoms. Those grains that adhered to this second tape were generally oriented with the tops exposed. We then performed SEM studies using the grains on this second tape.

SEM images of four representative grains are shown in Figure 11. Panels (a) and (b) were collected at a magnification of ~ 1000 and panels (c) and (d) at a magnification of ~ 3300. Ion-induced surface modification is clearly visible in each image. Panel (a) shows the formation of a relatively flat facet with some cone-like structures toward the back end of the grain. Panel (b) shows a smaller facet and greater formation of cone-like structures. In panels (c) and (d), the cone-like portion continues to increase as the facets portion decreases. These two panels also show that the cone-like structures have a wide variety of dimensions and can develop with or without a facet. We find that the sizes of the cones vary from tens of nanometers to tens of micrometers. We attribute the size differences to differing regions of crystallinity within the polycrystalline grains. The half angle for the cones varies from ~ 10° – 40°. These findings are consistent with the ion-induced surface topography observed in earlier Cu slab studies with similar fluences [23, 64, 65]. Based on these and other experimental studies [49, 67, 68], we expect that the facet surface is parallel to the ion beam direction and that the cones point to the direction of the ion beam origin.

ACCEPTED MANUSCRIPT
Journal of Applied Physics
AIP Publishing
This is the author's peer reviewed, accepted manuscript. However, the online version of record will be different from this version once it has been copyedited and typeset.
PLEASE CITE THIS ARTICLE AS DOI: 10.1063/5.0336473

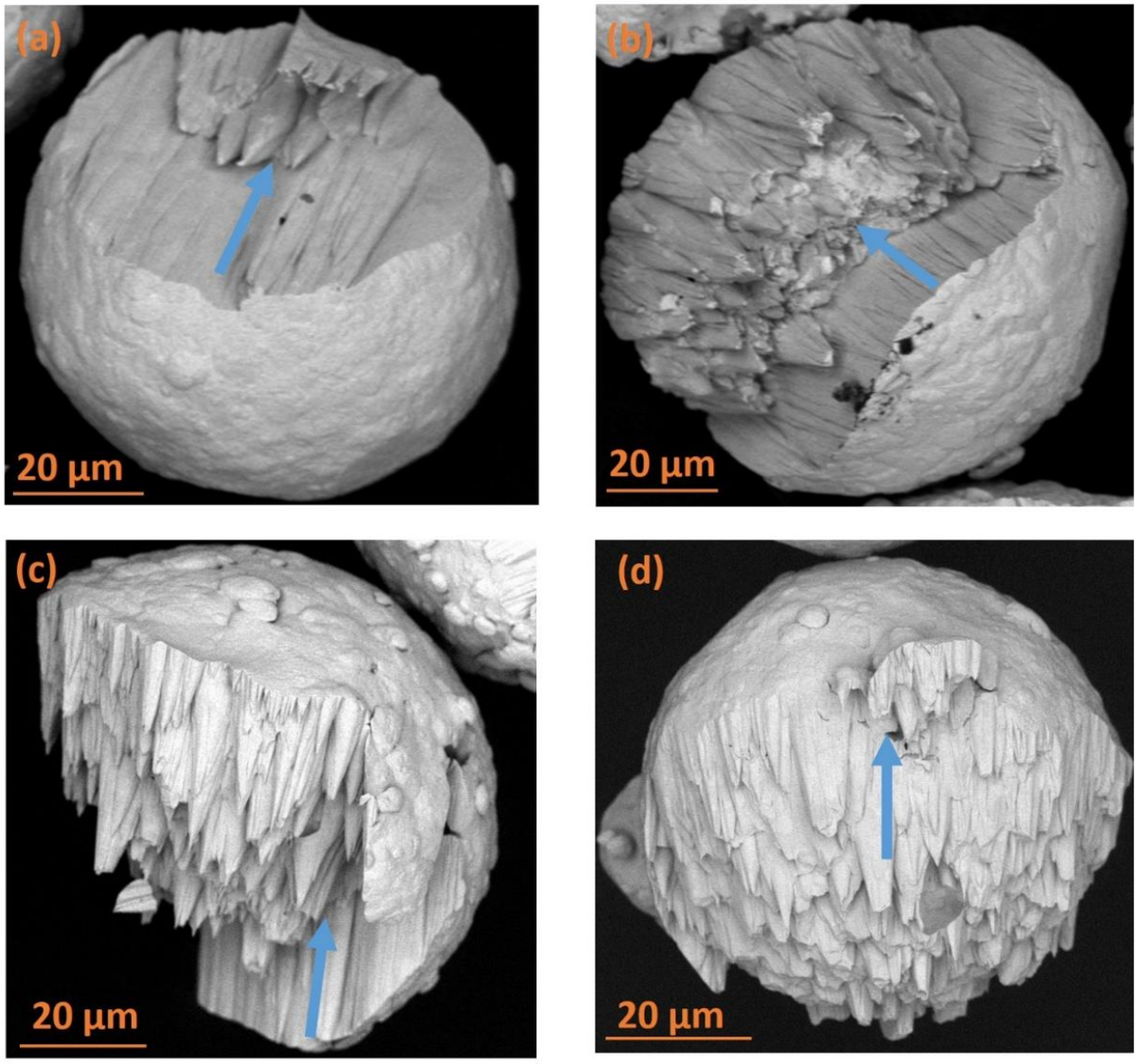



**Fig. 11.** SEM images for four representative Cu grains after irradiated by $(1.61 \pm 0.16) \times 10^{18}$ ions of 20 keV $Kr^+$ at incident angle of $\theta_i = 45°$. The images were collected on a Phenom XL using 5 keV primary electrons in the backscattered electron mode at a magnification of (a) ×970, (b) ×960, (c) ×3200 and (d) ×3400. The ion irradiation results in erosion of the grain, forming facets and cone-like structures out of the initial spherical grains. The blue arrows show the inferred ion beam direction.

ACCEPTED MANUSCRIPT
Journal of Applied Physics
AIP Publishing
This is the author's peer reviewed, accepted manuscript. However, the online version of record will be different from this version once it has been copyedited and typeset.
PLEASE CITE THIS ARTICLE AS DOI: 10.1063/5.0336473

Surface structure has been shown experimentally [14, 15, 18 – 20, 23, 49 – 51, 55, 57–61] and theoretically [21, 22, 55, 60, 66 – 68] to affect both the total sputtering yield and the angular distribution of the yields from flat slabs, rough surfaces, compressed pellets, and fuzzy surfaces. This is a consequence of two competing effects. Surface modification increases the local incidence angle and correspondingly increases the sputtering yield. However, the structure formed can also result in enhanced shadowing and redeposition of the ejecta. There is an additional effect in powders, namely, erosion of the tops of the grains in the uppermost layer of the powder, which correspondingly reduces the shadowing of the ejecta and thereby increases the escaping sputtering yield. The measured $Y_E/Y_F = 0.675 \pm 0.160$ indicates that surface modification is not sufficient to overcome the overall shadowing effects in the Cu powder as compared to flat Cu slab. This is to be contrasted with the W fuzz, where the layer of fuzz was slowly eroded as a function of ion fluence [49]. Eventually, the erosion formed a slab with a rough surface of cones pointing toward the ion beam origin. Not surprisingly, as a function of fluence, the sputtering yield approached that of the flat slab, but with a reduced yield in the forward direction. A similar reduction of sputtering in the forward direction was seen in our earlier Cu slab study, which we attributed to ion-induced surface roughness [23].

The role of ion-induced surface modification can be further explored in Figure 12, which presents the simulated-to-measured ratios of the doubly differential escaping sputtering yields for Cu powder, $(\mathrm{d}Y/\mathrm{d}\Omega)_s/(\mathrm{d}Y/\mathrm{d}\Omega)_m$. The figure demonstrates that there is no single scaling factor that will bring the simulated and measured results onto one another. We attribute this to the additional complexities introduced by ion-induced surface modifications. For example, for $\theta_i = 75°$, the simulations predict a larger sputtering yield in the forward direction than is seen in the measurements. This is likely due to the formation of cone-like structures that enhance shadowing in the forward direction.

We have not attempted, at this time, to incorporate ion-induced surface modification into our simulations. Our simulations can thus be considered static, where every incident ion sees a pristine surface. In the future, we will explore the possibility of dynamic simulations that incorporate surface modification into the model. However, Figure 11 demonstrates the complexity of the structures formed and, by inference, of incorporating this into the simulation.

It is worth noting, though, that the generally good agreement between our experimental and theoretical results indicates that surface modification of a loose powder does not significantly affect the sputtering process. We attribute this to the geometry of the ever-present interconnected voids being the factor controlling the escaping sputtering yield. This hypothesis is supported by our finding in [22] that the total escaping sputtering yield is a simple function of the porosity of the powder. This is also to be contrasted with sputtering from a fuzzy surface, where ion erosion eventually removes the fuzz, converting the target into a rough surface slab, and increasing the sputtering yield by over an order of magnitude [49].

ACCEPTED MANUSCRIPT
Journal of Applied Physics
AIP Publishing
This is the author's peer reviewed, accepted manuscript. However, the online version of record will be different from this version once it has been copyedited and typeset.
PLEASE CITE THIS ARTICLE AS DOI: 10.1063/5.0336473

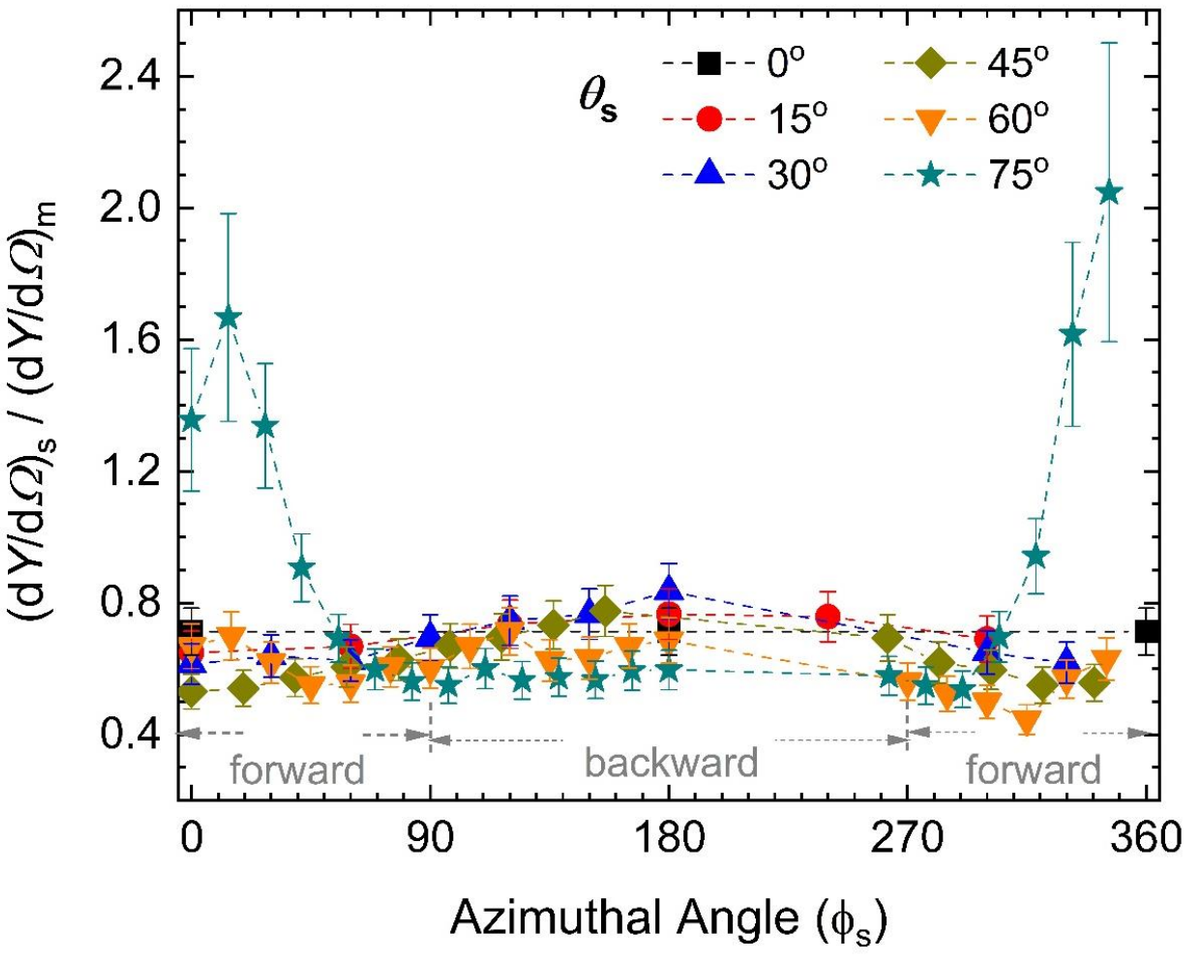



**Fig. 12.** The simulated-to-measured ratios of the doubly differential escaping sputtering yields for Cu powder, $(dY/d\Omega)_s$ / $(dY/d\Omega)_m$. The $(dY/d\Omega)_m$ are from Fig. 7(a), while the $(dY/d\Omega)_s$ are from Fig. 7(c). The $Kr^+$ ions traveled from $\phi_s = 180°$ toward $\phi_s = 0°$, at $\theta_i = 45°$. Relative to the ion velocity vector, the forward and backward sputtering directions are noted in the figure.

ACCEPTED MANUSCRIPT
Journal of Applied Physics
AIP Publishing
This is the author's peer reviewed, accepted manuscript. However, the online version of record will be different from this version once it has been copyedited and typeset.
PLEASE CITE THIS ARTICLE AS DOI: 10.1063/5.0336473

## 5 Conclusions

We have measured the absolute doubly differential angular escaping sputtering yield from a loose Cu powder produced by 20 keV $Kr^+$ ions impacting an incidence angle of 45°. We measured a total sputtering yield of 15.8 ± 2.0 atoms $ions^{-1}$. Under identical conditions, we measured the total sputtering yield from a flat Cu slab and found 23.4 ± 4.7 atoms $ion^{-1}$ [23]. The resulting powder-to-slab ratio of 0.675 ± 0.160 indicates that shadowing plays an important role in determining the escaping sputtering yield from a powder.

The measured ejecta lobe from the powder is backward directed, with respect to the incident ion velocity vector. This is distinctly different from the nearly normal ejecta lobe that is expected at an impact energy of 20 keV, where secondary knock-on collisions dominate the ejecta process and which is what was observed in our previous measurement with a Cu slab [23]. We attribute the backward-directed ejecta lobe to the interconnected voids of the Cu powder creating a preferred direction for the ejecta to escape the powder. Ions can penetrate through the interconnected voids of the powder, causing sputtering from underlying grains. These atoms are most likely to escape the powder if they are ejected roughly toward the origin of the incident ions, while ejecta in other directions are more likely to be shadowed by neighboring grains. Our experimental findings differ significantly from the normal distribution previously used in the literature for sputtering from a regolith.

We have also compared our powder simulations, using a multiscale Monte Carlo model that we have developed [22], to our experimental results. The model takes into account the effects of the granular roughness and of the porous structure formed by the interconnected voids in the powder. Overall, we find good qualitative agreement between the simulations and the experimental results. The simulated total sputtering yield is 10.5 atoms $ion^{-1}$, resulting in a theoretical-to-experimental ratio of 0.664 ± 0.084. We attribute this difference to ion-induced surface modifications reducing the peak heights of the topmost layer of the grains, thereby reducing shadowing of the ejecta and increasing the experimental yield above predictions. Surface modifications are not yet included in the simulations.

The simulations also show good qualitative agreement with the experimental results for the doubly differential angular sputtering yield. The simulations predict an ejecta lope enhanced in the backward direction, as was found in the measurements. In addition, both the simulations and the experimental results displayed the expected mirror symmetry with respect to the incidence plane. They also demonstrated that the ejecta lobe is not cylindrically symmetric around any axis.

Lastly, we have compared our results to published experimental and theoretical works for flat surfaces, rough surfaces, pressed pellets, and fuzzy surface. Our findings indicate that ion sputtering from loose powders is distinctly different from that of flat surfaces, rough surfaces, and pressed powders, which we interpret as being due to the lack of interconnected voids in these latter three targets. We do find some similarities with fuzzy surfaces but these disappear once ion erosion has removed the fuzz layer and converted the target into a rough surface. In summary, the geometry of the ever-present interconnected voids appears to be the dominant factor controlling the sputtering yield of powders; and accurately accounting for the total sputtering yield and the angular distribution of the ejecta from a powder needs to take this into account.

ACCEPTED MANUSCRIPT
Journal of Applied Physics
AIP Publishing
This is the author's peer reviewed, accepted manuscript. However, the online version of record will be different from this version once it has been copyedited and typeset.
PLEASE CITE THIS ARTICLE AS DOI: 10.1063/5.0336473

**Acknowledgements**

This work was supported, in part, by the NASA Solar System Workings grant 80NSCC22K0099. We also acknowledge support from NIH S10OD016219-01 for setting up the automated weighing system and from NSF-MRI 1919563 for the support of the scanning electron microscopy. S.V. acknowledges the support of ANR, France of the TEMPETE project (grant No. ANR-17-CE31-0016) and the support of CNES, France, for the BepiColombo mission. B. A. C.-G., J. R. L., and L. S. M. were supported, in part, by the NSERC Discovery Grant and the CSA Research Opportunities in Space Sciences program awards. This research was supported by the International Space Science Institute (ISSI) in Bern, through ISSI International Team project #616 "Multi-scale Understanding of Surface-Exosphere Connections (MUSEC)". We thank F. Leblanc for stimulating discussions.

**Declaration of Conflict of Interest**

The authors declare that they have no known competing financial interests or personal relationships that could have appeared to influence the work reported in this paper.

**Author Contributions**

**Caixia Bu:** Conceptualization (supporting), Data curation (lead); Formal analysis (equal); Funding acquisition (supporting); Investigation (equal); Methodology (equal); Project administration (supporting); Resources (equal); Software (supporting); Supervision (supporting); Validation (equal); Visualization (equal); Writing – original draft (lead); Writing – review & editing (equal). **Sebastien Verkercke**: Conceptualization (supporting), Data curation (supporting); Formal analysis (equal); Investigation (equal); Methodology (equal); Resources (equal); Software (lead); Supervision (supporting); Validation (equal); Visualization (equal); Writing – original draft (supporting); Writing – review & editing (equal). **Deborah Berhanu**: Data curation (supporting); Formal analysis (supporting); Investigation (equal); Methodology (equal); Resources (equal); Validation (supporting); Visualization (supporting); Writing – review & editing (supporting). **Benjamin C. Bostick:** Conceptualization (supporting), Data curation (supporting); Formal analysis (supporting); Funding acquisition (supporting); Investigation (equal); Methodology (supporting); Project administration (supporting); Resources (equal); Supervision (supporting); Validation (supporting); Writing – review & editing (supporting). **Steven. N. Chillrud:** Conceptualization (supporting); Data curation (supporting); Formal analysis (equal); Funding acquisition (supporting); Investigation (supporting); Methodology (supporting); Resources (equal); Supervision (supporting); Validation (equal); Visualization (supporting); Writing – review & editing (supporting). **Benjamin A. Clouter-Gergen:** Data curation (supporting); Formal analysis (equal); Investigation (supporting); Methodology (equal); Resources (equal); Software (supporting); Validation (supporting); Writing – review& editing (supporting). **Denton S. Ebel:** Conceptualization (supporting); Funding acquisition (supporting); Investigation (supporting); Methodology (supporting); Project administration (supporting); Writing – review & editing (supporting). **Isabel Hahn**: Investigation (supporting); Methodology (supporting); Software (supporting). **George E. Harlow:** Conceptualization (supporting); Funding acquisition (supporting); Investigation (supporting); Methodology (supporting); Writing – review & editing (supporting). **Pierre-Michel Hillenbrand:** Conceptualization (supporting); Data curation

ACCEPTED MANUSCRIPT
Journal of Applied Physics
AIP Publishing
This is the author's peer reviewed, accepted manuscript. However, the online version of record will be different from this version once it has been copyedited and typeset.
PLEASE CITE THIS ARTICLE AS DOI: 10.1063/5.0336473

(supporting); Formal analysis (supporting); Investigation (supporting); Methodology (supporting); Writing – review & editing (supporting). **Dmitry A. Ivanov:** Data curation (supporting); Formal analysis (supporting); Investigation (supporting); Methodology (supporting); Software (supporting); Writing – review & editing (supporting). **Jesse R. Lewis:** Data curation (supporting); Formal analysis (supporting); Investigation (supporting); Methodology (supporting); Software (supporting); Validation (supporting); Writing – review & editing (supporting). **Liam S. Morrisse**y: Conceptualization (supporting), Data curation (supporting); Formal analysis (equal); Funding acquisition (supporting); Investigation (equal); Methodology (equal); Resources (equal); Software (equal); Supervision (supporting); Validation (equal); Visualization (equal); Writing-original draft (supporting); Writing – review & editing (equal). **James M. Ross:** Data curation (supporting); Formal analysis (equal); Investigation (equal); Methodology (equal); Resources (equal); Validation (equal); Visualization (supporting); Writing – review & editing (supporting). **Xavier Urbain:** Conceptualization (supporting); Data curation (supporting); Formal analysis (supporting); Investigation (supporting); Methodology (supporting); Writing – review & editing (supporting). **Daniel. W. Savin:** Conceptualization (lead); Data curation (supporting); Formal analysis (equal); Funding acquisition (lead); Investigation (equal); Methodology (equal); Project administration (lead); Resources (equal); Software (supporting); Supervision (lead); Validation (equal); Visualization (equal); Writing-original draft (supporting); Writing – review & editing (equal).

## Data Availability

The data that support the findings of this study are available within the article.

## References

1. D Depla. "Sputter deposition with powder targets: An overview". Vacuum 184, 109892 (2021) https://doi.org/10.1016/j.vacuum.2020.109892

2. T. Ohshima, "Sputtering Deposition with Low Cost Multi-Element Powder Targets," in *IEEE Open Journal of Nanotechnology*, vol. 4, pp. 172-180 (2023). https://doi.org/10.1109/OJNANO.2023.3327997

3. S. Yu, Y. Zhao, G. Zhao, Q. Liu, B. Yao, and H. Liu, "Review on preparation technology and properties of spherical powders," Int. J. Adv. Manuf. Technol. 132, 1053–1069 (2024). https://doi.org/10.1007/s00170-024-13442-w.

4. B. Hapke, "Space weathering from Mercury to the asteroid belt", J. Geophys. Res.,106 10039–10074 (2001). https://doi.org/10.1029/2000JE001338

5. C. J. Bennett, C. Pirim, and T. M. Orlando, "Space-Weathering of Solar System Bodies: A Laboratory Perspective", Chem. Rev. 113(12),9086–9150 (2013). https://doi.org/10.1021/cr400153k

6. D. L. Domingue, C. R. Chapman,R. M. Killen,T. H. Zurbuchen,J. A. Gilbert, M. Sarantos, M. Benna, J. A. Slavin,D. Schriver, P. M. Trávníček, T.M. Orlando, A. L. Sprague, D. T. Blewett, J. J. Gillis-Davis, W. C. Feldman,D. J. Lawrence, G. C. Ho, D. S. Ebel,L. R. Nittler, F. Vilas,

ACCEPTED MANUSCRIPT
Journal of Applied Physics
AIP Publishing
This is the author's peer reviewed, accepted manuscript. However, the online version of record will be different from this version once it has been copyedited and typeset.
PLEASE CITE THIS ARTICLE AS DOI: 10.1063/5.0336473

C. M. Pieters, S. C. Solomon,C . L. Johnson, R. M. Winslow, J. Helbert, P. N. Peplowski, S. Z. Weider, N. Mouawad, N. R. Izenberg, and W. E. McClintock, "Mercury's Weather-Beaten Surface: Understanding Mercury in the Context of Lunar and Asteroidal Space Weathering Studies", Space Sci. Rev. 181,121–214 (2014). https://doi.org/10.1007/s11214-014-0039-5

7. C. M. Pieters, S. K. Noble, "Space weathering on airless bodies", J. Geophys. Res.: Planets 121, 1865-1884 (2016), https://doi.org/10.1002/2016JE005128

8. P. Wurz, U. Rohner, J. A. Whitby, C. Kolb, H. Lammer, P. Dobnikar, J. A. Martín-Fernández, "The lunar exosphere: The sputtering contribution", Icarus 191(2), 486 – 496 (2007), https://doi.org/10.1016/j.icarus.2007.04.034

9. C. A. Schmidt, F. Leblanc, K. Reardon, R. M. Killen, D. E. Gary, and K. Ahn, "Absorption Spectroscopy of Mercury's Exosphere During the 2016 Solar Transit," in LPI Editorial Board (ed.), *Mercury: Current and Future Science of the Innermost Planet*, vol. 2047 of LPI Contributions, 6022 (2018).

10. H. Lammer, M. Scherf, Y. Ito, A. Mura, A. Vorburger, E. Guenther, P. Wurz, N. V. Erkaev, and P. Odert, "The Exosphere as a Boundary: Origin and Evolution of Airless Bodies in the Inner Solar System and Beyond Including Planets with Silicate Atmospheres", Space Sci. Rev. 218, 15 (2022). https://doi.org/10.1007/s11214-022-00876-5

11. D. Gamborino, A. Vorburger, and P. Wurz, "Mercury's subsolar sodium exosphere: an ab initio calculation to interpret MASCS/UVVS observations from MESSENGER", Ann. Geophys. 37, 455–470 (2019). https://doi.org/10.5194/angeo-2018-109

12. P. Wurz, S. Fatemi, A. Galli, J. Halekas, Y. Harada, N. Jäggi, J. Jasinski, H. Lammer, S. Lindsay, M. N. Nishino, T. M. Orlando, J. M. Raines, M. Scherf, J. Slavin, A. Vorburger, and R. Winslow, "Particles and Photons as Drivers for Particle Release from the Surfaces of the Moon and Mercury", Space Sci. Rev. 218(3), 10 (2022), https://doi.org/10.1007/s11214-022-00875-6

13. R. M Killen, L. S. Morrissey, M. H. Burger, R. J. Vervack, O. J. Tucker, and D. W. Savin, "The influence of surface binding energy on sputtering in models of the sodium exosphere of Mercury", Planet. Sci. J. 3:139(13pp) (2022). https://doi.org/10.3847/PSJ/ac67de

14. R. Behrisch (ed.), 1981, Sputtering by Particle Bombardment I: Physical Sputtering of Single-Element Solids (Berlin: Springer).

15. R. Behrisch & W. Eckstein (eds.), 2007, Sputtering by Particle Bombardment: Experiments and Computer Calculations from Threshold to MeV Energies (Berlin: Springer).

16. B. Rauschenbach, 2022, Low-Energy Ion Irradiation of Materials: Fundamentals and Application (Cham, Switzerland: Springer).

17. B. Hapke, W. Cassidy, "Is the Moon really as smooth as a billiard ball? Remarks concerning recent models of sputter-fractionation on the lunar surface", Geophys. Res. Lett. 5 (4), 297-300 (1978). https://doi.org/10.1029/GL005i004p00297

ACCEPTED MANUSCRIPT
Journal of Applied Physics
AIP Publishing
This is the author's peer reviewed, accepted manuscript. However, the online version of record will be different from this version once it has been copyedited and typeset.
PLEASE CITE THIS ARTICLE AS DOI: 10.1063/5.0336473

18. M. J. Loeffler, C. A. Dukes, R. A. Baragiola, "Irradiation of olivine by 4 keV He+: Simulation of space weathering by the solar wind", J. Geophys. Res. Planets 114(E3) (2009). https://doi.org/10.1029/2008JE003249

19. H. Biber, J. Brötzner, N. Jäggi, P. S. Szabo, J. Pichler, C. Cupak, C. Voith, B. Cserveny, A. Nenning, A. Mutzke, M. V. Moro, D. Primetzhofer, K. Mezger, A. Galli, P. Wurz, and F. Aumayr, "Sputtering Behavior of Rough, Polycrystalline Mercury Analogs", Planet. Sci. J. 3:271 (10pp) (2022). https://doi.org/10.3847/PSJ/aca402

20. J. Brötzner, H. Biber, P. S. Szabo, N. Jäggi, L. Fuchs, A. Nenning, M. Fellinger, G. Nagy, E. Pitthan, D. Primetzhofer, A. Mutzke, R. A. Wilhelm, P. Wurz, A. Galli, and F. Aumayr, "Solar wind erosion of the Lunar regolith is suppressed by surface morphology and regolith properties", Commun. Earth Environ. 6, 560 (2025) https://doi.org/10.1038/s43247-025-02546-0

21. T. A. Cassidy, R. E. Johnson, "Monte Carlo model of sputtering and other ejection processes within a regolith", Icarus176 (2), 499 – 507 (2005). https://doi.org/10.1016/j.icarus.2005.02.013

22. S. Verkercke, D. Berhanu, C. Bu, B. Clouter-Gergen, F. Leblanc, J. R. Lewis, L. S. Morrissey, and D. W. Savin, "theoretical ion sputtering yields from loose powders using a multiscale Monte Carlo approach", J. Appl. Phys. 139, 145302 (2026). https://doi.org/10.1063/5.0316828

23. C. Bu, L. S. Morrissey, B. C. Bostick, M. H. Burger, K. P. Bowen, S. N. Chillrud, D. L. Domingue, C. A. Dukes, D. S. Ebel, G. E. Harlow, P.-M. Hillenbrand, D. A. Ivanov, R. M. Killen, J. M. Ross, D. Schury, O. J. Tucker, X. Urbain, R. Zhang, and D. W. Savin, "Absolute doubly differential angular sputtering yields for 20 keV $Kr^+$ on polycrystalline Cu", J. Appl. Phys. 135, 035302 (2024). https://doi.org/10.1063/5.0184417

24. C. Bu, B. C. Bostick, S. N. Chillrud, D. L. Domingue, D. S. Ebel, G. E. Harlow, R. M. Killen, D. Schury, K. P. Bowen, P.-M. Hillenbrand, X. Urbain, R. Zhang, and D. W. Savin, "Laboratory Simulations of Solar Wind Ion Irradiation on the Surface of Mercury", 52nd Lunar and Planetary Science Conference, Abstract #5248, page 2093.

25. C. D. Moak, H. E. Banta, J. N. Thurston, J. W. Johnson, and R. F. King, "Duo Plasmatron Ion Source for Use in Accelerators", Rev. Sci. Instrum. 30, 694 (1959). https://doi.org/10.1063/1.1716726

26. D. G. Seely, H. Bruhns, D. W. Savin, T. J. Kvale, E. Galutschek, H. Aliabadi, and C. C. Havener, "Rotating dual-wire beam profile monitor optimized for use in merged-beams experiments", Nucl. Instrum. Methods Phys. Res., Sect. A 585, 69 (2008). https://doi.org/10.1016/j.nima.2007.10.041

27. M. M. Mahmoud, "Characterization of the Native Oxide Shell of Copper Metal Powder Spherical Particles", Materials 15(20),7236 (2022). https://doi.org/10.3390/ma15207236

28. "Reduction of copper(II) oxide by hydrogen", https://rsc.li/3Edk0bv

ACCEPTED MANUSCRIPT
Journal of Applied Physics
AIP Publishing
This is the author's peer reviewed, accepted manuscript. However, the online version of record will be different from this version once it has been copyedited and typeset.
PLEASE CITE THIS ARTICLE AS DOI: 10.1063/5.0336473

29. M. E. Straumanis, and L. S. Yu. "Lattice parameters, densities, expansion coefficients and perfection of structure of Cu and of Cu–In α phase." Foundations of Crystallography 25(6), 676-682 (1969). https://doi.org/10.1107/S0567739469001549

30. J. F. Moulder, W. F. Stickle, P. E. Sobol, & K. D. Bomben. "Handbook of X-ray Photoelectron Spectroscopy", edited by J. *Chastain (Perkin-Elmer, Eden Prairie, MN, 1992)*, *118*.

31. S. Tanuma, C. J. Powell, and D. R. Penn (1991). "Calculations of electorn inelastic mean free paths. II. Data for 27 elements over the 50–2000 eV range". Surf. Interface Anal. 17(13), Pages 911-926. https://doi.org/10.1002/sia.740171304

32. S. Tougaard, and B. Jørgensen. "Inelastic background intensities in XPS spectra", Surface Science, 143(2-3), 482-494 (1984). https://doi.org/10.1016/0039-6028(84)90554-5.

33. M. H. Engelhard, D. R. Baer, A. Herrera-Gomez, P. M. A. Sherwood. "Introductory guide to backgrounds in XPS spectra and their impact on deter-mining peak intensities." J. Vac. Sci. Technol. A 38, 063203 (2020). https://doi.org/10.1116/6.0000359

34. I. Platzman, R. Brener, H. Haick, and R. Tannenbaum. "Oxidation of polycrystalline copper thin films at ambient conditions." J. Phys. Chem. C 112(4), 1101-1108 (2008). https://doi.org/10.1021/jp076981k

35. T. H. Fleisch, and G. J. Mains. "An XPS study of the UV reduction and photochromism of MoO3 and WO3." J. Chem. Phys. 76(2), 780-786 (1982). https://doi.org/10.1063/1.443047

36. S. Suzuki, Y. Ishikawa, M. Isshiki, and Y. Waseda. "Native oxide layers formed on the surface of ultra high-purity iron and copper investigated by angle resolved XPS." Materials Transactions, JIM 38, no. 11, 1004-1009 (1997). https://doi.org/10.2320/matertrans1989.38.1004

37. B. R. Strohmeier. "An ESCA method for determining the oxide thickness on aluminum alloys". Surf. Interface Anal. 15, 51-56 (1990). https://doi.org/10.1002/sia.740150109

38. P. Dubot, D. Jouset, V. Pinet, F. Pellerin, and J. Langeron , "Simulation of the LMM Auger Spectra of Copper". Surf. Interface Anal. 12, 99 (1998). https://doi.org/10.1002/sia.740120207

39. K. Kanayat and S. Okayama, "Penetration and energy-loss theory of electrons in solid targets", J. Phys. D: Appl. Phys. 5, 43 – 57 (1972).

40. H. E. Swanson, H. F. McMurdie, M. C. Morris, and E. H. Evans, "Standard X-ray diffraction powder patterns". Natl. Bur. Stand. U.S. Circ. 359 (1953).

41. J. F. Xu, W. Ji, Z. X. Shen, S. H. Tang, X. R. Ye, D. Z. Jia, X. Q. Xin, "Preparation and Characterization of CuO Nanocrystals, Journal of Solid State Chemistry", 147 (2), 516-519 (1999). https://doi.org/10.1006/jssc.1999.8409

42. B. D. Cullity, and S. R. Stock Stock. Elements of X-Ray Diffraction. Prentice Hall; Hoboken, NJ, USA: 2001.

ACCEPTED MANUSCRIPT
Journal of Applied Physics
AIP Publishing
This is the author's peer reviewed, accepted manuscript. However, the online version of record will be different from this version once it has been copyedited and typeset.
PLEASE CITE THIS ARTICLE AS DOI: 10.1063/5.0336473

43. Q. Lei, L. Huang, J. Yin, B. Bavaasuren, Y. Yuan, X. Dong, Z.-P. Wu, X. Wang, K. X. Yao, X. Lu, and Y. Han. "Structural evolution and strain generation of derived-Cu catalysts during CO2 electroreduction". Nat. Commun. 13, 4857 (2022). https://doi.org/10.1038/s41467-022-32601-9

44. A. P.Thompson, H. M. Aktulga, R. Berger, D. S. Bolintineanu, W. M. Brown, P. S. Crozier, P. J. in't Veld, A. Kohlmeyer, S. G. Moore, T. D. Nguyen, R. Shan, M. J. Stevens, J. Tranchida, C. Trott, S. J. Plimpton, "LAMMPS-a flexible simulation tool for particle-based materials modeling at the atomic, meso, and continuum scales", Computer Physics Communications 271, 108171 (2022).

45. K. L. Johnson, K. Kendall, & A. Roberts. "Surface energy and the contact of elastic solids". Proceedings of the royal society of London. A. mathematical and physical sciences, 324(1558), 301-313 (1971). https://doi.org/10.1098/rspa.1971.0141

46. P. S. Szabo, A. R. Poppe, H. Biber, A. Mutzke, J. Pichler, N. Jaggi, A. Galli, P. Wurz, and F. Aumayr. "Deducing lunar regolith porosity from energetic neutral atom emission." Geophys. Res. Lett. 49(21), e2022GL101232 (2022). https://doi.org/10.1029/2022GL101232

47. S. Verkercke, J. Y. Chaufray, F. Leblanc, E. M. Bringa, D. Tramontina, L. Morrissey, & A. Woodson. "Effects of Airless Bodies' Regolith Structures and of the Solar Wind's Properties on the Backscattered Energetic Neutral Atoms Flux". Planet. Sci. J. 4(10), 197 (2023). https://doi.org/10.3847/PSJ/acf6bd

48. A. Mutzke, U. V. Toussaint, W. Eckstein, R. Dohmen, & K. Schmid (2024). SDTrimSP Version 7.00.

49. R. Stadlmayr, P.S. Szabo, D. Mayer, C. Cupak, T. Dittmar, L. Bischoff, S. Möller, M. Rasiński, R.A. Wilhelm, W. Möller, F. Aumayr, "Sputtering of nanostructured tungsten and comparison to modelling with TRI3DYN", J. Nucl. Mater. 532 (2020), https://doi.org/10.1016/j.jnucmat.2020.152019

50. J. A. M. McDonnell, and R. P. Flavill (1974), "Solar wind sputtering on the lunar surface: Equilibrium crater densities related to past and present microparticle influx rates," Lunar Sci., III, 2441–2449.

51. D. Nishijima, N. J. Baldwin, R. P. Doerner, & J. H. Yu, "Sputtering properties of tungsten 'fuzzy'surfaces." J. Nucl. Mater. 415(1), S96-S99. (2011). https://doi.org/10.1016/j.jnucmat.2010.12.017

52. M. J. Baldwin, & R. P. Doerner, "Formation of helium induced nanostructure 'fuzz'on various tungsten grades." J. Nucl. Mater. 404(3), 165-173 (2010) https://doi.org/10.1016/j.jnucmat.2010.06.034

53. H. Iwakiri, K. Yasunaga, K. Morishita, and N. Yoshida, "Microstructure evolution in tungsten during low-energy helium ion irradiation", J. Nucl. Mater. 283, 1134 – 1138 (2000). https://doi.org/10.1016/S0022-3115(00)00289-0

ACCEPTED MANUSCRIPT
Journal of Applied Physics
AIP Publishing
This is the author's peer reviewed, accepted manuscript. However, the online version of record will be different from this version once it has been copyedited and typeset.
PLEASE CITE THIS ARTICLE AS DOI: 10.1063/5.0336473

54. S. Kajita, W. Sakaguchi, N. Ohno, N. Yoshida, and T. Saeki, "Formation process of tungsten nanostructure by the exposure to helium plasma under fusion relevant plasma conditions", Nucl. Fusion 49,095005 (6pp) (2009). http://dx.doi.org/10.1088/0029-5515/49/9/095005

55. C. Cupak, P. S. Szabo, H. Biber, R. Stadlmayr, C. Grave, M. Fellinger, J. Brötzner, R.A. Wilhelm, W. Möller, A. Mutzke, M.V. Moro, F. Aumayr, "Sputter yields of rough surfaces: Importance of the mean surface inclination angle from nano- to microscopic rough regimes", Applied Surface Science 570, 151204 (2021). https://doi.org/10.1016/j.apsusc.2021.151204

56. Y. Yamamura, T. Takiguchi, & H. Tawara, (1990), Data Compilation of Angular Distributions of Sputtered Atoms, NIFS-DATA-1 (Nagoya, Japan: National Institute for Fusion Science of Japan).

57. H. Gnaser, "Energy and Angular Distribution of Sputtered Species", in Sputtering By Particle Bombardment, edited by Raiser Behrisch and Wolfgane Eckstein (Springer, Berlin, Germany, 2007), p. 231 – 301

58. Y. Yamamura, and K. Muraoka. "Over-cosine angular distribution of sputtered atoms at normal incidence" Nucl. Instrum. Methods Phys. Res. B 42(2), 175 – 181 (1989). https://doi.org/10.1016/0168-583X(89)90704-0

59. H. H. Andersen, B. Stenum, T. Sarensen and H. J. Whitlow, "Angular distribution of particles sputtered from Cu, Pt, and Ge targets by keV Ar+ ion bombardment", Nucl. Instr. Meth. B 6, 459 – 465 (1985). https://doi.org/10.1016/0168-583X(85)90003-5

60. A. Afkir, M. A. El Fqih, L. Jadoual, V. Shulaga, A. Kaddouri. "Angular distribution of particles sputtered from a copper target by 5-keV Kr ions: experimental and simulation study" Surf. Interface Anal. 53, 792–797 (2012). https://doi.org/10.1002/sia.6980

61. Y. Yamamura, C. Mößner, H. Oechsner, "Angular distributions of sputtered atoms from ion-bombarded surfaces", Radiat. Eff. 105, 31 (1987). http://dx.doi.org/10.1080/00337578708210060

62. B. W. Hapke, "A theoretical photometric function for the lunar surface." J. Geophys. Res. 68(15), 4571-4586 (1963). https://doi.org/10.1029/JZ068i015p04571

63. J. Brötzner, H. Biber, P. S. Szabo, N. Jäggi, L. Fuchs, A. Nenning, M. Fellinger, G. Nagy, E. Pitthan, D. Primetzhofer, A. Mutzke, R. A. Wilhelm, P. Wurz, A. Galli, and F. Aumayr, "Sputter Yields of the Luna Surface: Experimental Validation and Numerical Modelling of Solar Wind Sputtering of Apollo 16 Soils", arXiv:2410.14450 https://doi.org/10.48550/arXiv.2410.14450

64. A. D. G. Stewart and M. W. Thompson. "Microtopography of surfaces eroded by ion-bombardment". J. Mater. Sci. 4, 56 (1969). https://doi.org/10.1007/BF00555048

65. J. L. Whitton, G. Carter, M. J. Nobes, & J. S. Williams, "The development of cones and associated features on ion bombarded copper." Radiation Effects, 32(3-4), 129-133. (1977)

ACCEPTED MANUSCRIPT
Journal of Applied Physics
AIP Publishing
This is the author's peer reviewed, accepted manuscript. However, the online version of record will be different from this version once it has been copyedited and typeset.
PLEASE CITE THIS ARTICLE AS DOI: 10.1063/5.0336473

66. M. A Makeev, and A.-L. Barabási. "Effect of surface morphology on the sputtering yields. II. Ion sputtering from rippled surfaces", Nucl. Instr. Meth. B 222 (3), 335-354 (2004). https://doi.org/10.1016/j.nimb.2004.02.028

67. D. P. Datta and T. K. Chini." Coarsening of ion-beam-induced surface ripple in Si: Nonlinear effect vs. geometrical shadowing". Phys. Rev. B 76, 75323 (2007). https://doi.org/10.1103/PhysRevB.76.075323

68. T. Basu, D.P. Datta, and T. Som, "Transition from ripples to faceted structures under low-energy argon ion bombardment of silicon: understanding the role of shadowing and sputtering". Nanoscale Res. Lett. 8, 1 (2013). https://doi.org/10.1186/1556-276X-8-289